2021-05

Hydro-sediment-morphodynamic processes of the baige landslide-induced barrier Lake, Jinsha River, China

Li, J

http://hdl.handle.net/10026.1/17643

1   **Hydro-Sediment-Morphodynamic Processes of the Baige Landslide-induced**

2   **Barrier Lake, Jinsha River, China**

3

4   Ji Li[a, b], Zhixian Cao[a *], Yifei Cui[c], Xuanmei Fan[d], Wenjun Yang[e],

5   Wei Huang[e], Alistair G. L. Borthwick[f]

6

7   [a] *State Key Laboratory of Water Resources and Hydropower Engineering Science, Wuhan*
8   *University, Wuhan 430072, China*;

9   [b] *Zienkiewicz Centre for Computational Engineering, College of Engineering, Swansea*
10   *University, Swansea SA1 8EN, UK*;

11   [c] *State Key Laboratory of Hydroscience and Engineering, Tsinghua University, Beijing*
12   *100084, China;*

13   [d] *State Key Laboratory of Geohazard Prevention and Geoenvironment Protection, Chengdu*
14   *University of Technology, Chengdu 610059, China*;

15   [e] *Changjiang River Scientific Research Institute, Wuhan 430010, China*;

16   [f] *Institute for Infrastructure and Environment, The University of Edinburgh, Edinburgh EH9*
17   *3FG, UK.*

18   *Corresponding author, Zhixian Cao, email address: zxcao@whu.edu.cn

19

20   **Highlights:**

21   ● The 2018 Baige landslide-induced barrier lake on the Jinsha River is investigated

22   ● The whole process is well reconstructed by a single 2D model for the first time

23   ● An artificial flood channel effectively alleviated downstream flood risk

24   ● Grains drive water during landslide dam formation, but water governs the outburst

25   ● Effects of upstream inflow discharge and initial landslide volume are revealed

26

Abstract

A large landslide impacting a river may cause a multi-phase chain of hazards, comprising landslide-generated waves, inundation as a barrier lake develops upstream a landslide dam arising from rapid sediment deposition, and downstream flooding due to barrier lake outburst. Two major landslides (each of volume ~ 10^7 m^3) occurred successively on 10th October and 3rd November 2018 at Baige village, Tibet, China. Both landslides led to a natural dam that completely blocked the Jinsha River, along with a barrier lake filled with upstream river inflow. Although the first barrier lake breached naturally, a significant quantity of residual material from the first landslide dam was left behind without being eroded. After the second landslide occurred, a flood channel was urgently constructed to facilitate an artificial breach of the barrier lake as it formed. The Baige landslide-induced barrier lake is unique as triggered by two successive landslides and outbursts a mere five weeks apart. Here a computational investigation is presented of the hydro-sediment-morphodynamic processes of the Baige barrier lake, using a recent 2D double layer-averaged two-phase flow model. This is the first modelling study of the whole field and whole processes for the formation and outburst of a landslide-induced barrier lake as well as the resultant floods, without evoking presumptions on dam breach (which have prevailed for decades and bear much uncertainty). The computed results agree well with field observations in terms of landslide-generated waves, landslide dam morphology, stage and discharge hydrographs at the dam site and downstream flood hydrographs. The artificial flood channel is shown to be effective for alleviating downstream inundation. Water and grain velocities are demonstrated to be distinct, characterizing the primary role of grains in landslide dam and barrier lake formation and the dominant role of water in barrier lake outburst and the resultant flood. Relatively low inflow discharge and large initial landslide volume favour landslide dam and barrier lake formation, but delay the outburst and downstream flood. The present 2D double layer-averaged two-phase model holds great promise for assessing future landslide-induced multi-hazard chains in rivers, and informing mitigation and adaptation strategies.

Keywords: landslide dam; landslide-generated waves; barrier lake outburst; flood; hydro-sediment-morphodynamic processes; double layer-averaged two-phase flow model

1. Introduction

Landslides are common geophysical mass events in mountainous regions, especially those with deep, narrow valleys (Costa and Schuster, 1988; Ermini and Casagli, 2003). A landslide impacting a river often produces a multi-hazard chain comprising landslide-generated waves, a landslide dam, a barrier lake, a lake outburst, and resultant floods, leading to spatial-temporal amplification of hazard (Carpignano et al., 2009; Fan et al., 2019a). More specifically, when a subaerial landslide impacts a narrow river valley, large amplitude water waves and active sediment transport can be generated. Due to rapid deposition of a huge amount of sediment, a landslide dam forms as the riverbed rapidly aggrades and then emerges from the water (Costa and Schuster, 1988; Van Asch et al., 1999). The resulting water waves may trigger further landslides and/or collapses of the opposite riverbank, entraining additional sediment into the river and facilitating landslide dam formation. As a consequence of sustained upstream inflow and significant water-level rise, the water impounded by a landslide dam usually creates a barrier lake, which may inundate upstream land and infrastructure. Owing to its rather loose structure, a landslide dam formed by granular materials can easily burst, leading to destructive downstream floods. Such outburst floods from a barrier lake consist of highly mobile water-sediment mixtures, capable of traveling long distances (sometimes beyond 100 km) at high velocity (exceeding 10 km/hr). These events can cause high numbers of casualties and severe infrastructural damage (Ermini and Casagli, 2003; Shang et al., 2003; Dai et al., 2005), due to their sudden onset, high magnitude discharge, long runout distance, and their tendency to flow along existing river channels where humans and property are concentrated (Carrivick, 2010; Cui et al., 2013).

79   Typical historical examples include the landslide dam outburst events in June 1786 at

80   the Dadu River, Sichuan, China, which is reported to have caused more than 100,000

81   fatalities (Dai et al., 2005; Lee and Dai, 2011), in October 1999 at the Poerua River, New

82   Zealand (Davis et al., 2007), in April-June 2000 at the Yigong Zangpo River, Tibetan, China

83   (Delaney and Evans, 2015), in May 2008 at Tangjiashan, Sichuan, China due to the

84   Wenchuang earthquake (Xu et al., 2009), and in October 2018 at Yarlung Tsangpo River in

85   Tibetan Plateau, China due to ice-avalanche (Chen et al., 2020). More recently, two major

86   landslides occurred successively on 10 October and 3 November 2018 (Fan et al., 2019b),

87   which created a natural dam that completely blocked the Jinsha River, followed by a barrier

88   lake filled by upstream runoff. On 12 October, the first barrier lake breached naturally with a

89   peak discharge of about 10,000 m^3/s (Cai et al., 2019). The residual landslide dam was

90   replenished with sediment from the second landslide on 3 November, forming a larger barrier

91   lake than the first. On 11 November, following the urgent construction of a flood channel, the

92   second barrier lake breached artificially with a peak discharge of 33,900 m^3/s.

93   Modelling the whole-process chain of a landslide-induced barrier lake flood is important

94   for two reasons. First, knowledge of the chain is useful in assessing the hazard and risk of

95   potential future landslide-induced barrier lake flood events. This is both salient and timely,

96   noting that climate change is promoting increased instability of high mountain slopes and has

97   accelerated increasing trends in the amount, intensity, and occurrence frequency of extreme

98   precipitation (Donat et al., 2013), which are likely to trigger more landslides. Second, the

99   whole-process chain is key to improving our understanding of such earth surface processes

100   that are prohibitively difficult to observe in nature owing to their sheer complexity. Physically,

101 a typical landslide-induced multi-hazard chain involves two distinct but intertwined processes:

102 aggradation through sediment deposition during landslide dam and barrier lake formation;

103 and degradation induced by sediment erosion during a barrier lake outburst and the

104 subsequent floods. Previous studies have mostly focused on one or two components of the

105 whole-process chain, whereas little work has been done on the whole-process chain

106 modelling.

107   Landslide dam and barrier lake formation represent the first part of the whole-process

108 chain. In general, existing models for resolving landslide dam and barrier lake formation can

109 be divided into two categories: discrete models and continuum models. Typical discrete

110 models like Smoothed Particle Hydrodynamics - SPH (Shi et al., 2016; Xu et al., 2020) and

111 Materials Point Method two-phase models (Bandara and Soga, 2015) can be directly used for

112 modelling landslide dam and barrier lake formation. Other examples include coupled Discrete

113 Element Method landslide models and fluid flow models based on computational fluid

114 dynamics (Zhao et al., 2017), Lattice-Boltzmann Method (Leonardi et al., 2016), as well as

115 coupled Discontinuous Deformation Analysis and SPH models (Wang et al., 2017, 2019). Yet,

116 excessive computational costs preclude applications of these models to real field-scale cases.

117 As far as continuum models are concerned, although 3D models are available (e.g., Hu et al.,

118 2020), double layer-averaged models hold great promise for resolving landslide dam and

119 barrier lake formation due to their ability to represent the two-way coupling between

120 landslide motions and water flows (Abadie et al., 2012) and to achieve a sensible balance

121 between theoretical integrity and applicability (Li et al., 2019). It should be emphasized that

122 double layer-averaged models are automatically applicable when there is only a single-layer

123   flow, either clear-water flow or water-sediment mixture flow. Recently, a 2D double

124   layer-averaged two-phase flow model (Li et al., 2020) has been proposed for landslide dam

125   and barrier lake formation, which employs one set of layer-averaged single-phase flow

126   equations to describe the upper clear-water flow layer and a second set of layer-averaged

127   two-phase flow equations to describe the subaerial or subaqueous water-sediment mixture

128   flow layer. This model incorporates multiple grain size, inter-phase and inter-grain size

129   interactions, unlike previous double layer-averaged models that involve a single-phase flow

130   assumption and assume a single grain size (e.g., Skvortsov and Bornhold, 2007; Liu and He,

131   2016; Si et al., 2018; Li et al., 2019) and that ignore mass exchange with the bed, sediment

132   mass conservation and steep slope effect (e.g., Skvortsov and Bornhold, 2007; Si et al., 2018).

133   It is noted that the double layer-averaged single-phase model by Liu and He (2016)

134   incorporated mass exchange with the bed, but incorrectly added a term for actual momentum

135   exchange with the bed (see statement by Cao et al. 2017), and assumed constant sediment

136   concentration, which is in conflict with the sediment mass conservation law.

137   Overtopping flow with subsequent dam erosion is the most common trigger for a barrier

138   lake outburst (Costa and Schuster, 1988). Over the past few decades, substantial effort has

139   been devoted to improving the understanding of the mechanisms underpinning a barrier lake

140   outburst and the subsequent flood (Cao et al., 2011b). Particular attention has been paid to

141   landslide dam breaching due to its governing role in the generation and propagation of the

142   downstream flooding. According to ASCE/EWRI (2011), dam breach models can be

143   categorized as parametric models, simplified physically based models, and detailed

144   physically based models. Parametric models are derived purely from data collected from a

145 series of documented breaching events (e.g., Walder and O'Connor, 1997; Xu and Zhang,

146 2009; Peng and Zhang, 2012). Simplified physically based models, such as NWS BREACH

147 (Fread, 1988), WinDAM (Temple et al., 2005), HR BREACH (Morris et al., 2009), DABA

148 (Chang and Zhang, 2010), and DLBreach (Wu, 2013), predict outflow hydrographs from a

149 breaching dam. The accuracy of such predictions hinges upon predefined model assumptions

150 (most critically, weir flow assumption) and physical input parameters. Detailed physically

151 based models (Wang and Bowles, 2006a, b; Faeh, 2007; Wang et al., 2008; Cao et al., 2011b,

152 c; Wu et al., 2012; Huang et al. 2012; Li et al. 2013) incorporate the physical mechanisms of

153 a dam breach. Discharge and stage hydrographs as well as breach development can be

154 resolved without predefining or constraining the evolution process. It is noted that in order to

155 predict outburst downstream floods, it is customary for the aforementioned parametric and

156 simplified physically-based dam breach models to be integrated with flood routing models,

157 e.g., FLO-2D (O'Brien et al., 1993), HEC-RAS (USACE, 2016), and BASEMENT (Vetsch et

158 al., 2018). In contrast, detailed physically based models can resolve flow and sediment

159 transport throughout the entire computational domain (ASCE/EWRI, 2011).

160 Integrated modelling refers to individual modelling of specific processes within a

161 whole-process chain, with sub-model outputs of a single process used at each subsequent step

162 as input to the next process sub-model. A general disadvantage of this approach is that

163 transitions between different processes are not straightforward (Worni et al., 2014), and one

164 sub-model output may not exactly fit the required input for the next sub-model. Concurrently,

165 integrated modelling hinges upon the capability of the sub-models involved. Liu and He

166 (2018) tried to model the whole-process chain of the Yigong landslide by integrating a double

167 layer-averaged single-phase model (Liu and He, 2016) for landslide dam and barrier lake

168 formation and a conventional single layer-averaged single-phase model (e.g., Cao et al., 2004)

169 for a dam breach and subsequent flood routing. Fan et al. (2020a) conducted an integrated

170 modelling study on the Baige landslide-induced multi-hazard chain using a MassFlow

171 sub-model for landslide movement, a DABA sub-model (Chang and Zhang, 2010) for dam

172 breaching, and a one-dimensional HEC-RAS sub-model for downstream flood routing.

173 Inevitably, the integrated model is constrained by the capability of each sub-model. For

174 instance, the MassFlow sub-model is a single layer-averaged single-phase flow model for

175 landslide movement, and so cannot resolve landslide-induced waves and barrier lake

176 formation that involve strong interactions between landslide motion and river flow.

177 Overall, a single state-of-the-art model that properly couples all physical processes is the

178 way forward (Worni et al., 2014). In this regard, a 2D double layer-averaged two-phase flow

179 model appears particularly attractive, noting that such a model has previously been applied

180 successfully to landslide dam and barrier lake formation caused by a landslide impacting a

181 river (Li et al., 2020), and that its single-phase predecessor was applied for a barrier lake

182 outburst and subsequent flood (Li et al., 2013). Here the hydro-sediment-morphodynamic

183 processes of the Baige landslide-induced multi-hazard chain are investigated using the model

184 of Li et al. (2020). First, we aim to benchmark the model against field observations of

185 landslide-generated waves, landslide dam morphology, stage and discharge hydrographs in

186 2018. The role of water and grains in the whole processes is evaluated. Second, we aim to

187 unravel the effects of inflow discharge and landslide volume on the multi-hazard chain as

188 unstable rock mass clusters in the source area of the Baige landslides may fail in the future,

189 characterizing potential for river damming and flooding (Fan et al., 2020a). To the authors'

190 knowledge, this is the first whole-field and whole-process modelling study of the Baige

191 landslide-induced multi-hazard chain using a single physically based model (Li et al., 2020),

192 unlike existing studies on a part of the whole-process chain (Hu et al., 2020; L. Zhang et al.,

193 2019; Zhong et al., 2020; Fan et al., 2020a). Most notably, the present work does not involve

194 presumptions regarding the onset of landslide dam outburst and of the breach/scour pattern

195 and discharge estimation by analogy to weir flow, which have prevailed for several decades

196 and bear excessive uncertainty.

197

2. Baige barrier lake

199 In 2018, the Jinsha River, the upper course of the Yangtze River, was blocked by two

200 successive landslides that occurred on 10 October and 3 November (Fig. 1). At 22:00 on 10

201 October (Beijing time, UTC + 8 throughout the paper), a large landslide occurred on the right

202 bank of the Jinsha River, at Baige village, located at the border between Sichuan Province

203 and Tibet Autonomous Region, China (98°42′17.98″ E 31°4′56.41″ N). The first landslide

204 had a total material volume of about 27.5 million m^3 (Cai et al. 2019), the majority of which

205 formed a landslide dam of bed length ~1500 m and crest width ~ 700 m (Fig. 2a), aligned

206 stream-wise and transverse respectively with the river. The dam crest elevation ranged from

207 3005 m above mean sea level at the left bank to 2931 m at the right bank. This landslide dam

208 completely blocked the Jinsha River, for the first time in recent history. As the inflow

209 discharge reached 1680 m^3/s (Cai et al., 2019), the water level rose rapidly, leading to the
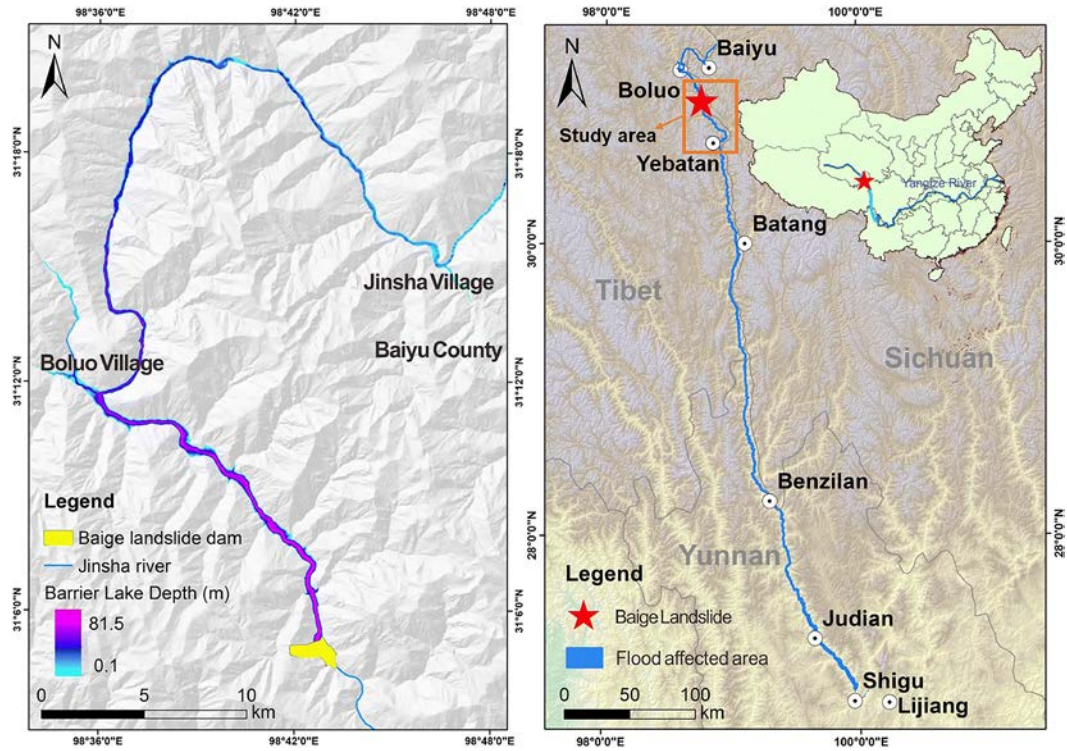
210   formation of a barrier lake, called the "10.10" Baige barrier lake. The landslide dam

211   overtopped naturally at 17:30, 12 October, and underwent breaching for about 21 hrs (Fig.

212   2b). Details of the breaching process have been documented as follows. The breaching flow

213   discharge was less than 100 m^3/s before 20:00 on October 12. By 00:45 on October 13, the

214   water level in the barrier lake reached a maximum of 2932.7 m above mean sea level,

215   corresponding to a water storage volume of 290 million m^3. The overflow increased

216   significantly after 01:00 on October 13. At 06:00 on October 13, the breaching flow peaked

217   at about 10,000 m^3/s (Cai et al. 2019). Afterwards, the breaching flow gradually attenuated

218   and returned to base flow by about 14:00 on October 13. The natural breach of the "10.10"

219   Baige barrier lake resulted in a flood that caused huge damage to towns in its downstream

220   path. Many houses, roads, and bridges were damaged or even destroyed, and more than

221   20,000 people had to be evacuated.

222   About 3 weeks after the natural breach of the first barrier lake, a second landslide, caused

223   by reactivation of residual material left behind by the first landslide, occurred at the same site

224   at 17:15 on 3 November. Landslide material was deposited on the earlier natural breaching

225   channel and blocked the Jinsha River once again (Fig. 3a). The second landslide had an initial

226   volume of about 3.5 million m^3, and an additional entrainment volume of about 8.5 million

227   m^3. The average height of the new landslide dam was 50 m higher than its predecessor, and

228   its lowest crest elevation was approximately 2966 m above mean sea level. With an incoming

229   flow discharge of about 800 m^3/s, the water level increased continuously, forming the

230   so-called "11.03" Baige barrier lake. As the second landslide had raised the overall height of

231   the landslide dam, the threat posed by the second barrier lake was higher than by the first lake.

232   To mitigate flood risk, an artificial flood channel, 220 m long, 15 m deep, 42 m top width,

233   and 3 m bottom width, was constructed at the lowest crest of the second landslide dam,

234   reducing its bed elevation to 2951 m (Fig. 3b). With this flood channel in place, the landslide

235   dam overtopped at 04:45 on 12 November, and the breaching process lasted over 50 hrs (Fig.

236   3c, d). The peak dam breach flow discharge reached 33,900 m^3/s at 18:20 on 12 November.

237   At the dam site, the discharge returned to a base flow level by 08:00 on 14 November. The

238   outburst flood destroyed many bridges along the Jinsha river including the Old Zhubalong

239   Jinsha Bridge connecting a key highway between Sichuan and Tibet, inundated numerous

240   towns, and led to the urgent evacuation of over 100,000 people.

241   The study area of the present work extends from approximately 6 km upstream of the

242   Baige landslide dam site to Yebatan gauging station (54 km downstream of the Baige

243   landslide dam site), and includes a ~ 60 km long reach of the Jinsha river (Fig. 1).

244

Fig. 1. Location of Baige barrier lake, Jinsha River, China (adapted from Fan et al., 2020a): (a) upstream areas inundated by barrier lake; (b) towns affected by downstream flooding (the orange box indicates the study area).
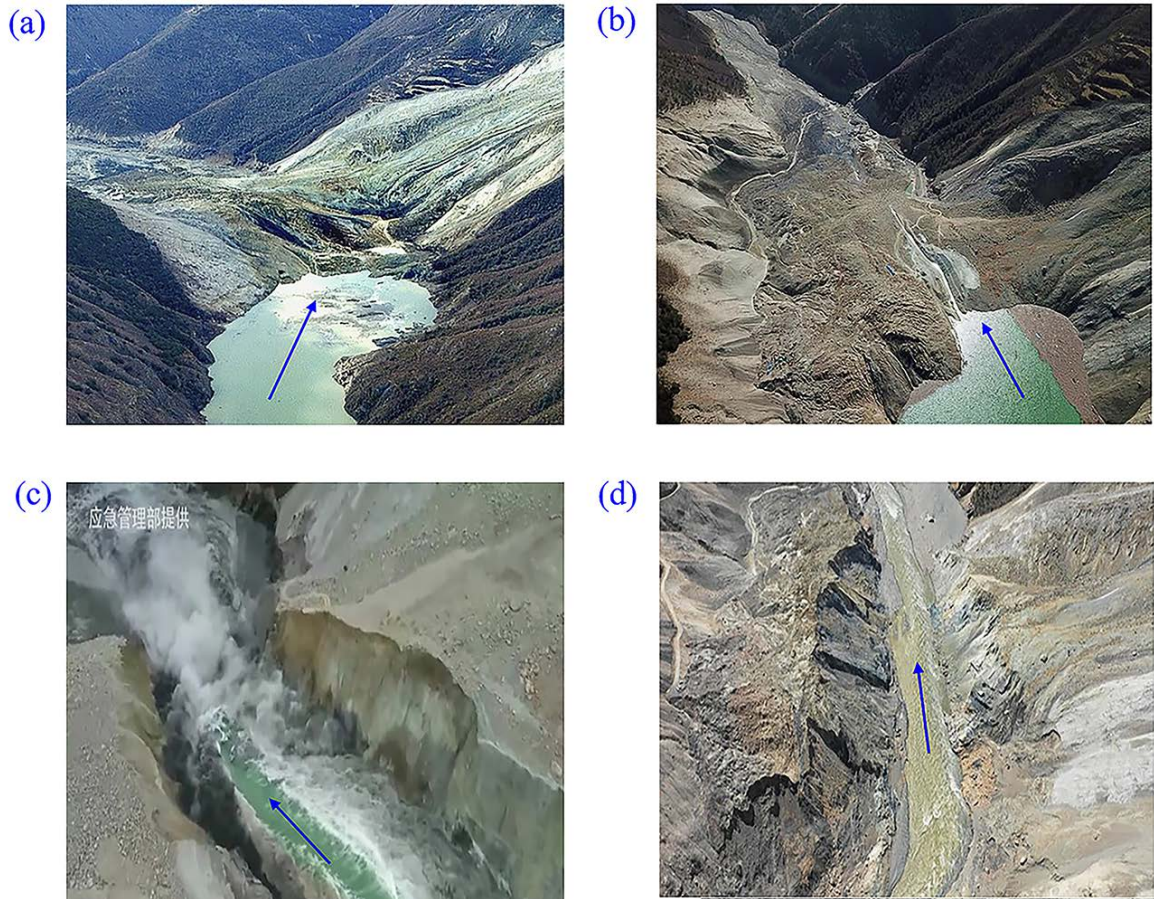
Fig.2. "10.10" Baige barrier lake: (a) formation; (b) after breaching. (photo courtesy of Chinanews.com).

Fig. 3. "11.03" Baige barrier lake: (a) formation; (b) with artificial flood channel; (c) during breaching; (d) after breaching (photo courtesy of a CCTV.com; b Red Star News; c Ministry of Emergency Management of China; d L. Zhang et al., 2019).

3. Modelling method

3.1. Mathematical model

A recent state-of-the-art 2D double layer-averaged two-phase model (Li et al., 2020) is used to resolve the whole-process chain concerning the Baige events, commencing from landslide-generated waves, to landslide dam and barrier lake formation as the landslide impacted the Jinsha river, and thence to the outburst of the barrier lake and subsequent flood propagation downstream.

14

266   Li et al. (2020) provide a detailed description of the 2D double layer-averaged two-phase

267   flow model equations, model closure, and the numerical algorithm. Briefly, the model has

268   been constructed according to continuum mechanics principles, and explicitly incorporates

269   multiple grain sizes, sediment mass conservation, mass exchange with the bed, and interphase

270   and inter-grain size interactions. To close the model, a set of relationships is introduced to

271   determine shear stresses, water entrainment, interaction forces, and sediment exchange fluxes.

272   It should be noted that all the closure relations used in the double layer-averaged two-phase

273   flow   model   have   been   established   in   the   general   field   of   shallow   water

274   hydro-sediment-morphodynamics. Although the model incorporates first-order factors, such

275   as gravitation, resistance, inter-phase and inter-grain size interactions, higher-order factors

276   such as non-Newtonian liquid viscous stress (Pudasaini, 2012), viscous particle resuspension

277   (Reeks and Hall, 2001) and shear-induced particle migration (Morris, 2009), are yet to be

278   included in the model.

279

280   *3.2. Model set-up*

281   In this study, in order to improve computational efficiency, the whole-process chain

282   concerning the Baige barrier lake events of 2018 has been divided into Phase I: "10.10"

283   Baige barrier lake event, and Phase II: "11.03" Baige barrier lake event. This is reasonable

284   given the more than three-week gap between the two events. For Phase I, the pre-sliding bed

285   topography was reconstructed using a 15m-resolution DEM (Digital Elevation Model). The

286   total duration of the Phase I simulation was 72 hrs, from 22:00 on 10 October to 22:00 on 13

287   October. For Phase II, the bed morphology resulting from the first event was used as the

288   initial bed topography. The total duration of the Phase II simulation was 260 hrs, from 17:15

289   on 3 November to 13:15 on 14 November. For each phase, time $t = 0$ s coincided with the

290   instant that the relevant landslide began to occur. The position and thickness of the initial

291   landslide body were estimated from the post-landslide field survey (Cai et al., 2019). Water

292   level elevation and velocity prior to landslide were determined by maintaining a constant

293   base flow at the inlet boundary. From the landslide deposit investigation by L. Zhang et al.

294   (2019), the bulk porosity $p = 0.45$, median grain size $d_{50} \approx 10$ mm, grain density $\rho_s =$

295   2700 kg/m^3. According to the grain size distribution measured by L. Zhang et al. (2019), the

296   sediment mixture was separated into two size fractions: $d_1 = 1$ mm (60%) and $d_2 = 20$ mm

297   (40%), with mean diameter d_m of 8.6 mm.

298   The friction angle $\delta = 35°$, the Manning coefficients for bed roughness $n_b = 0.04$

299   m$^{-1/3}$ s, interface roughness $n_w = 0.01$ m$^{-1/3}$ s, the empirical weighting parameter $\varphi = 0.65$,

300   and the modification coefficient $\phi = 1$ were calibrated to the observed landslide dam

301   morphology and breaching flow discharge after the first landslide, and then directly applied

302   to the second barrier lake event. The inflow discharge of clear water (Q_i) was kept constant

303   throughout each phase of the simulation, i.e. $Q_i = 1680$ m^3/s for Phase I, and $Q_i = 800$

304   m^3/s for Phase II. The clear water velocity and layer thickness at the inlet were determined by

305   the method of characteristics. At the outlet, either the method of characteristics was used to

306   obtain updated values of the flow variables under subcritical flow conditions, or zero flow

307   variable gradients imposed for supercritical flows (Liang and Borthwick, 2009). Within the

308   time period considered, the landslides did not reach the computational boundaries, and so the

309   landslide boundary conditions were simply set at the initial static state. The overall

310   dimensions of the computational domain were 35 km × 20 km, and a fixed uniform mesh of

311   spatial increment 20 m was adopted. The $x-$ and $y-$ directions are aligned north-south

312   and east-west, respectively. The Courant number, Cr, was set to 0.4.

313   To quantify the error of a numerical solution as compared with measured data, the

314   non-dimensional discrepancy is defined based on the L^1 norm

315
$$L_f^1 = \frac{\sum_{i=1}^{N} abs(\overline{f}_i - \widehat{f}_i)}{\sum_{i=1}^{N} \overline{f}_i} \tag{1}$$

316   where the symbol f represents physical variables such as bed deformation thickness and

317   flow discharge; N is the number of measured data; $\overline{f}$ denotes numerical solution,

318   whereas $\widehat{f}$ represents measured data.

319

320   **4. Results**

321   *4.1. Phase I: the "10.10" Baige barrier lake event*

322   First, the Phase I "10.10" Baige barrier lake event is reconstructed, commencing from

323   landslide-generated waves, and landslide dam and barrier lake formation, through to the

324   barrier lake outburst and downstream flood propagation. Multiple anticipated scenarios

325   concerning effects of inflow discharge and initial landslide volume are considered, and

326   sensitivity analysis to evaluate the effects of bed friction coefficient $\tan \delta$ and Manning

327   roughness coefficient n_b are conducted.

328

4.1.1. Landslide movement and wave generation

330   According to the field survey and analysis of broadband seismograms undertaken by Z.

331   Zhang et al. (2019), the peak velocity of the landslide during its runout was recorded at the

332   nearest seismological station within 100 s. Fig. 4 shows the predicted evolution of landslide

333   velocity U_m $(=\sqrt{u_m^2 + v_m^2}$, where u_m and v_m are the layer-averaged horizontal velocity

334   components of the water-sediment mixture in the landslide in the $x-$ and $y-$directions.

335   After initiation, the sliding mass accelerates eastwards down the hillslope alongside the

336   Jinsha river, and first arrives at the water surface at $t=$ 20 s when the landslide front has a

337   speed of approximately 62 m/s and has not yet reached its maximum (Fig. 4c). The rear of the

338   landslide continues to push the front further into the river channel. By $t=40$ s, most of the

339   landslide material has impacted the river and is generating waves; meanwhile, the direction of

340   travel of the landslide material is diverted downstream with a maximum sliding mass speed

341   of approximately 72 m/s (Fig. 4d). The predicted maximum speed is close to alternative

342   computed results ($\approx$ 75 m/s) by Hu et al. (2020) using Flow-3D software. Subsequently, the

343   landslide gradually decelerates, resulting in decreased landslide speed and thickness due to

344   rapid deposition of the landslide material (Fig. 4(e-f)). Notably, at $t=$ 100 s, landslide

345   movement has almost come to a halt with its maximum speed falling below 2 m/s, echoing

346   the findings from the field survey and analysis of broadband seismogram signals (Z. Zhang et

347   al., 2019). By $t=$ 900 s, the landslide thickness has almost vanished, indicating that most of

348   the landslide material has been deposited on the riverbed and a landslide dam formed.

349   After the landslide impacts the Jinsha River, the river surface is disturbed, generating

350   large waves. These landslide-generated waves are initially forced by inertia of the high-speed

351   sliding mass, with water displaced soon after the sliding mass crashes into the river channel.

352   Along with the sliding mass, the generated waves tend to run up the opposite bank in the

353   direction of the landslide run-out. After a landslide-generated wave moves to its maximum

354   elevation on the opposite bank, water then flows back into the watercourse. As evident in

355   Table 1, the computed results provide a satisfactory match to field observations by Cai et al.

356   (2019) of the maximum run-up elevation of the landslide-generated waves and the size of the

357   area affected by the waves on the opposite bank. Fig. 5 shows predicted water level

358   hydrographs at Points A, B, and C along the river course, which indicate the propagation of

359   landslide-generated waves downstream and upstream of the "10.10" Baige landslide in the

360   Jinsha River. The hydrographs indicate that the waves propagate as bores with steep front and

361   flatting rear. The maximum elevation of the water level at point B rise to 2950 m, exceeding

362   the initial water surface by about 90 m. The maximum water level reaches 2919 m at point A

363   and 2900 m at point C, indicating that the landslide-generated waves may produce more

364   serious hazards in the downstream zone. The initial rises in water level at points B and C

365   occur almost simultaneously, showing that the main entry position of the sliding mass is

366   situated in the near upstream zone.

367
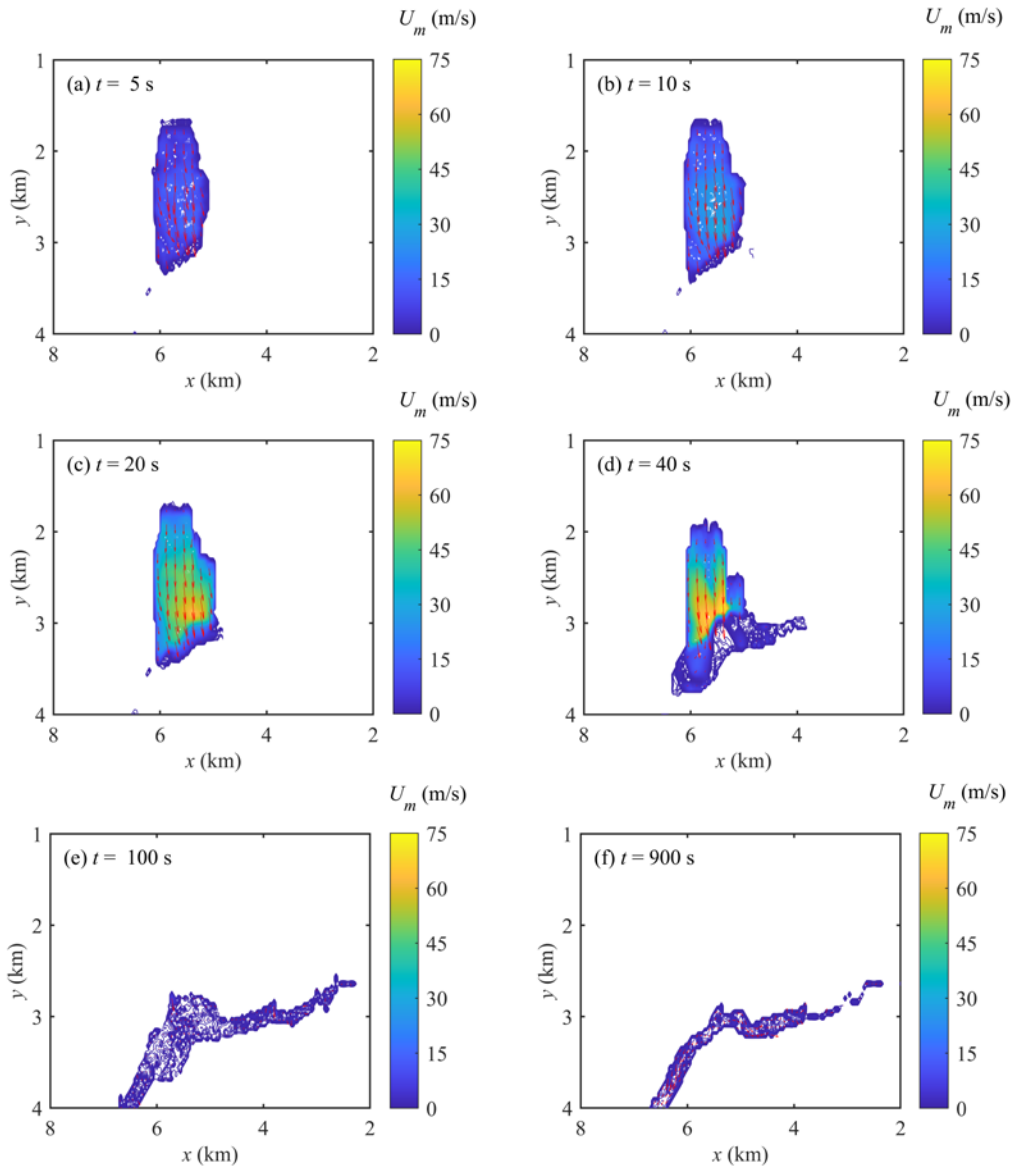
Fig. 4. Phase I "10.10" Baige landslide impacting Jinsha river: model predictions of landslide velocity field at times $t =$ (a) 5 s, (b) 10 s, (c) 20 s, (d) 40 s, (e) 100 s, and (f) 900 s.
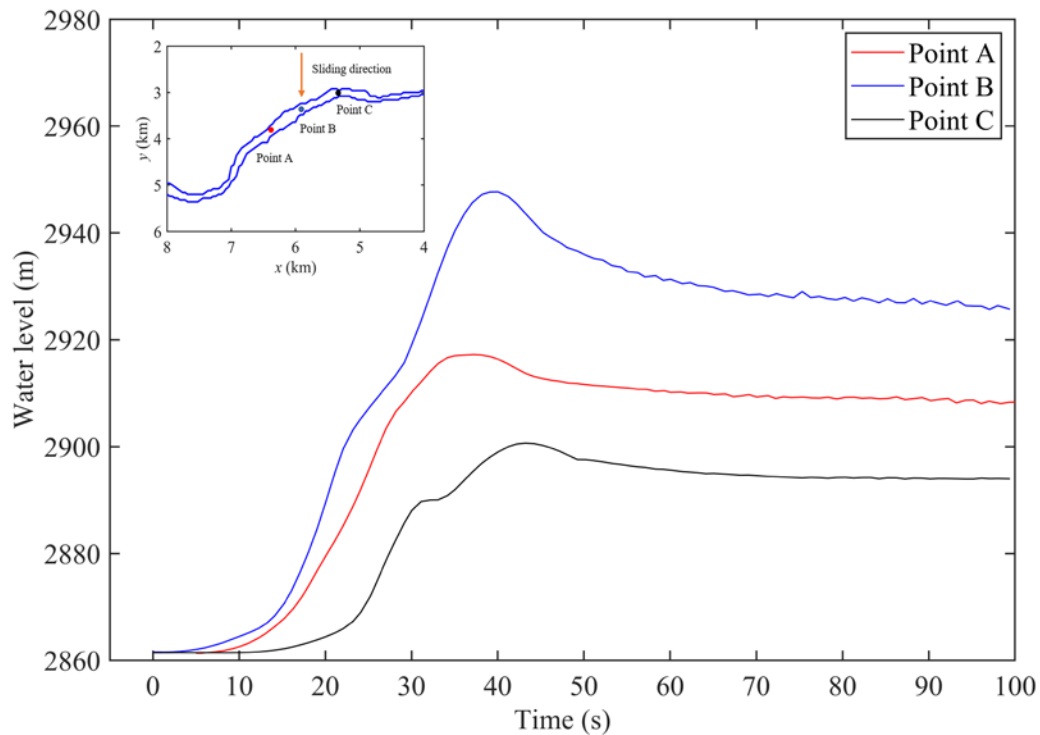
Table 1 "10.10" Baige landslide-generated wave run-up on the opposite bank

Results		Computed	Measured
Maximum elevation (m)		3051.8	3065
Affected region	Length (m)	1690.5	1500
	Area (10^4 m^2)	36.3	37.6

[*] Observed data from Cai et al. (2019)

Fig. 5. Phase I "10.10" Baige landslide-generated waves: predicted water level hydrographs at three locations in the Jinsha river near Baige, Sichuan, China.

4.1.2. Landslide dam and barrier lake formation

Fig. 6(a) displays the landslide dam morphology, represented by deformation of the original bed, at $t = 900$ s. In general, the dam body is higher at the left bank than at the right bank. The landslide dam body is divided into four longitudinal sections (I, II, III, and IV) in the river flow direction, following Cai et al. (2019). Table 2 shows the consistent agreement obtained between the computed and measured elevations above sea level and lengths of the four longitudinal sections. Fig. 6(b) presents the predicted cross-section thickness profile at A-A' (Fig. 6a) of the landslide dam along the river, along with measured data from Fan et al. (2020a). Although discrepancies are appreciable between the present modelling and observed

21

data, the landslide dam morphology predicted by the present model is in good overall

agreement with the measured data. In particular, the computed maximum dam height is 84.2

m, slightly higher than the measured value of 81.4 m. Quantitatively, the value of the L^1
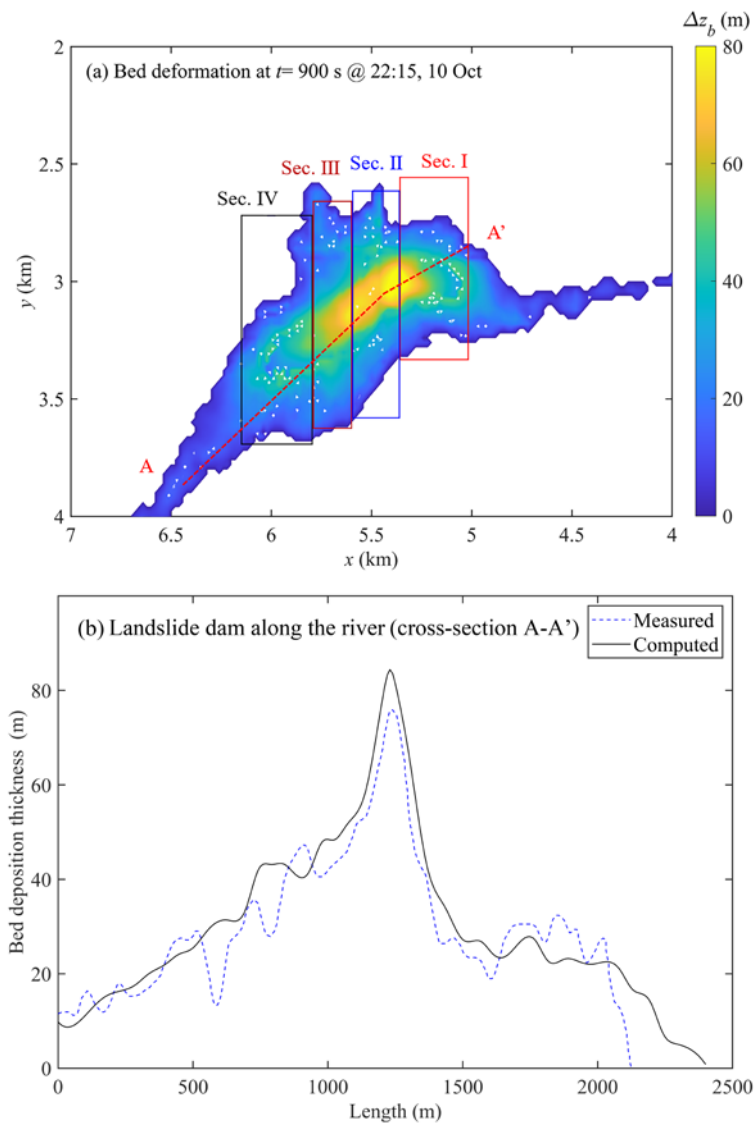
norm for bed deposition thickness $L^1_{bd} = 12.45\%$

Fig. 6. "10.10" Baige landslide dam geometry: (a) bed deformation at $t = 900$ s predicted by present model; and (b) cross-section profile of landslide dam in the original river stream-wise direction (A-A'): model prediction (solid line) and measured data from Fan et al. (2020a) (dashed line).

Table 2 Summary of "10.10" Baige landslide dam morphology

Section	Elevation (m)		Length (m)	
	Computed	Measured[*]	Computed	Measured[*]
I	2996~3012	2998~3005	410	412
II	2965~2978	2973~2977	220	206
III	2963~2981	2977	250	215
IV	2943~2953	2948~2951	450	421

[*] Observed data from Cai et al. (2019)

Fig. 7 shows the landslide dam and barrier lake formation process due to the "10.10" Baige landslide impacting the Jinsha river as the water layer depth h_w, landslide layer thickness h_s, and bed deformation Δz_b evolve with time. The landslide first accelerates down the hillslope ramp (Figs. 7 a1-a2, b1-b2), then directly crashing into the river, and forcing the water to run up the opposite bank while generating large water waves (Figs. 7 a3, b3 and c3). Later, most of the landslide material is rapidly deposited on the riverbed, forming a landslide dam (Figs. 7 a4, b4 and c4). Meanwhile, water waves significantly erode the opposite riverbank (Fig. 7 c4), entraining more sediment into the river and further facilitating landslide dam formation. Soon after the landslide dam forms, a barrier lake is created due to the river blockage, and the volume of this lake gradually increases thereafter due to the sustained upstream inflow, as shown in Figs. 7(a5 and a6). During this stage, waves propagate back and forth upstream of the dam, affected by a combination of the sustained river inflow and the sudden arrival of the dam. By contrast, waves downstream of the landslide dam exhibit one-way propagation downstream adding to riverbed erosion.
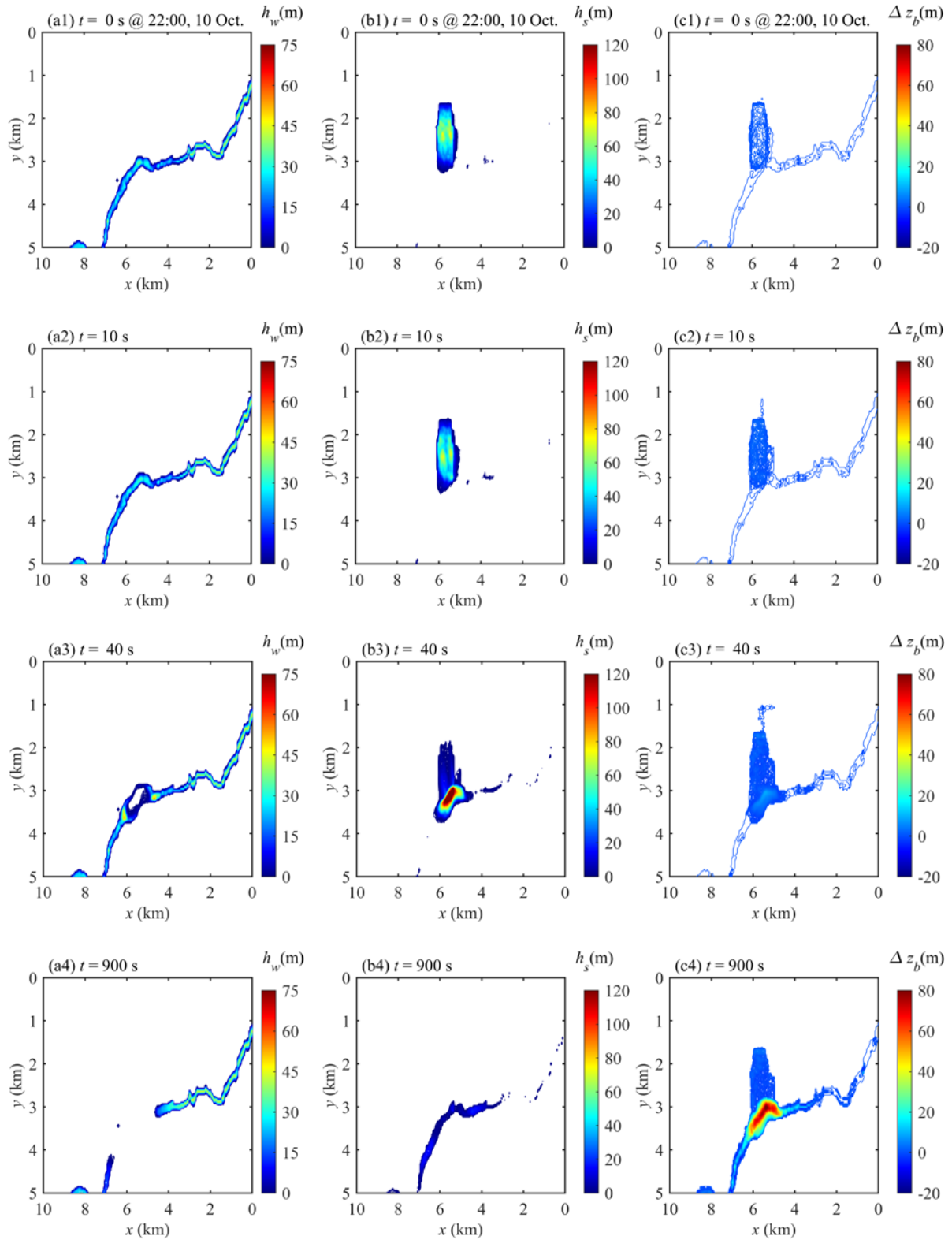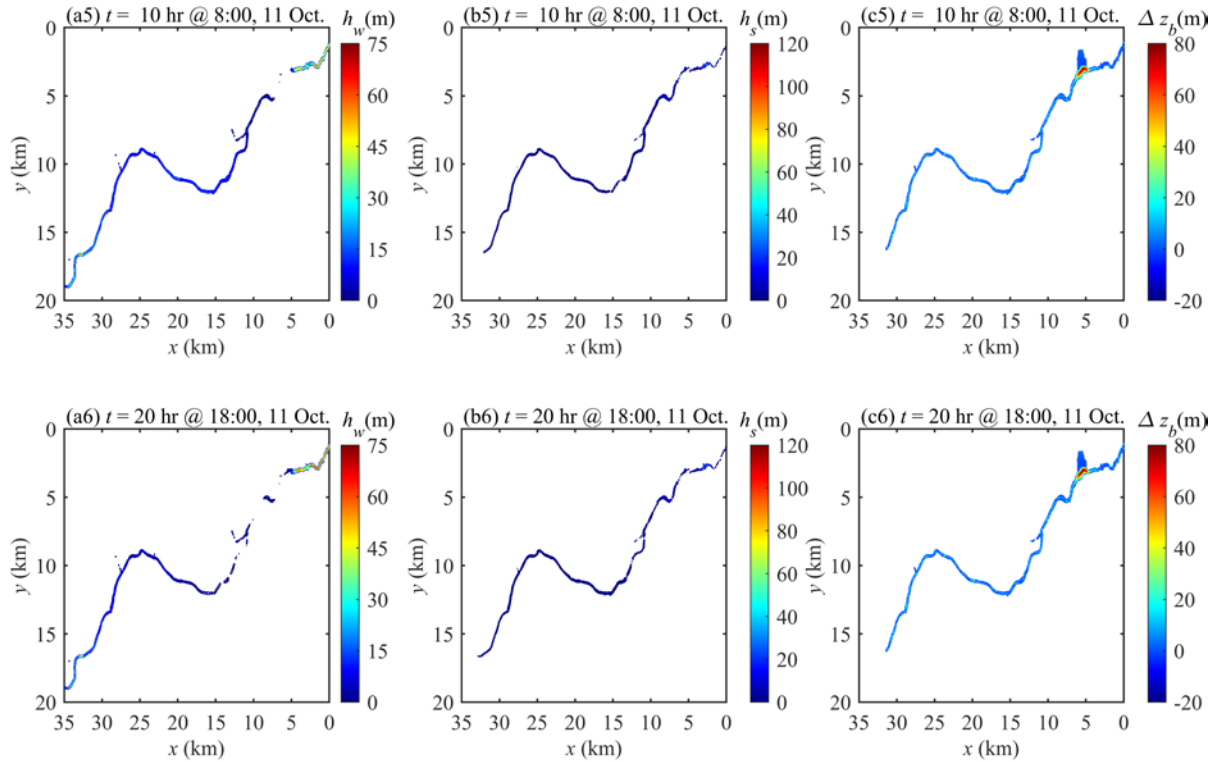
416

Fig. 7. "10.10" Baige landslide dam and barrier lake formation: (a1-a6) depth of water layer; (b1-b6) landslide thickness; and (c1-c6) bed deformation.

4.1.3. Barrier lake outburst and the resultant flood

The "10.10" Baige landslide dam was overtopped naturally at 17:30, 12 October. This overtopping flow increased drastically at midnight (00:00, 13 October), reached a peak value of approximately 10,000 m³/s at about 06:00 on 13 October, and returned to base flow at 14:30 on 13 October. Fig. 8(a) shows the excellent agreement obtained between the predicted breach flow hydrograph with the observed data reported by Cai et al. (2019). The predicted peak discharge of 9691 m³/s occurs at 05:45 on 13 October, and is slightly below the observed peak of 10,000 m³/s and 15 mins earlier than the observed time (06:00 on 13 October). The present model offers improved accuracy over simplified physically-based models (such as that of L. Zhang et al., 2019). Fig. 8(b) presents computed and measured

431　discharge hydrographs at the downstream gauging station at Yebatan, along with computed

432　sediment volume output time series. Again, the model predictions closely match the measured

433　data. It can be seen that the peak discharge is attenuated along the river. At Yebatan, the

434　predicted peak discharge is 7941 m^3/s at 8:12 on 13 October, whereas the observed maximum

435　discharge is 7822 m^3/s at 8:40 on 13 October. Thereafter, the discharge gradually reduces to

436　base flow. By the end of "10.10" Baige barrier lake event, it is estimated that 3.48×10^6 m^3 of

437　sediments have been flushed downstream due to the outburst flood, thus the bulk aggradation

438　in the river course between Baige dam site and Yebatan amounts to 2.4×10^7 m^3 [$= 2.75 \times 10^7$

439　m^3 (total volume of "10.10" Baige landslide) $- 3.48 \times 10^6$ m^3 (sediment volume output)]. The

440　L^1 norms for breaching flow discharge hydrograph $L^1_{Q_b}$ and flow discharge hydrograph at

441　Yebatan gauging station L^1_Q are respectively 15.3% and 16.25%.

442　　　Fig. 9 presents the simulated time series of water levels at the barrier lake and several

443　sites downstream of the landslide dam. Due to bursting of the barrier lake, its water level,

444　indicated by the dashed line, decreases by over 27 m, which is consistent with the observed

445　value in excess of 20 m reported by media. Water levels at locations downstream of the

446　landslide dam site generally experience a sharp increase due to the arrival of the outburst

447　flood and then a relatively flatter decrease with time. Similar to the peak discharge (Fig. 8),

448　the amplitude of water level rise becomes increasingly attenuated with distance along the

449　river (the value decreases from 28 m at a location 5 km downstream of the dam to 13.5 m at
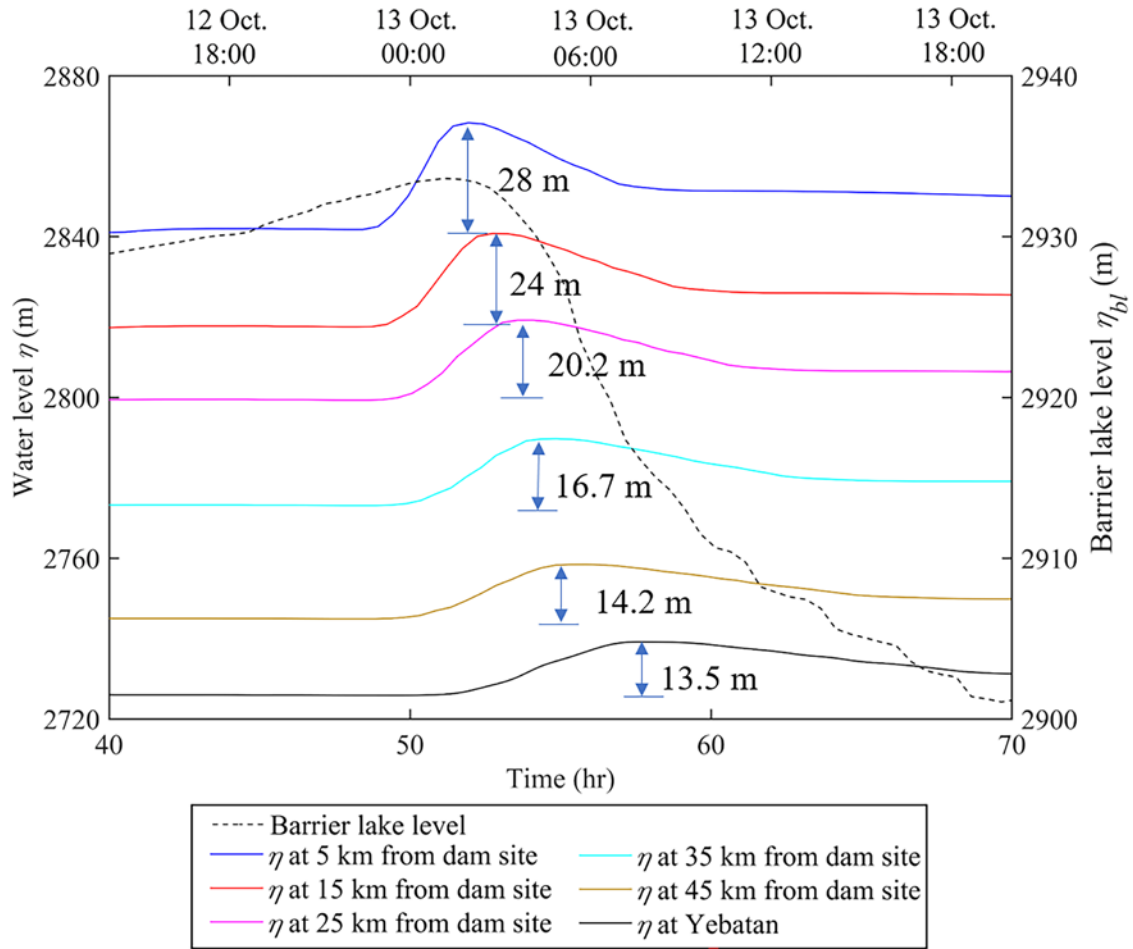
450　Yebatan).

451
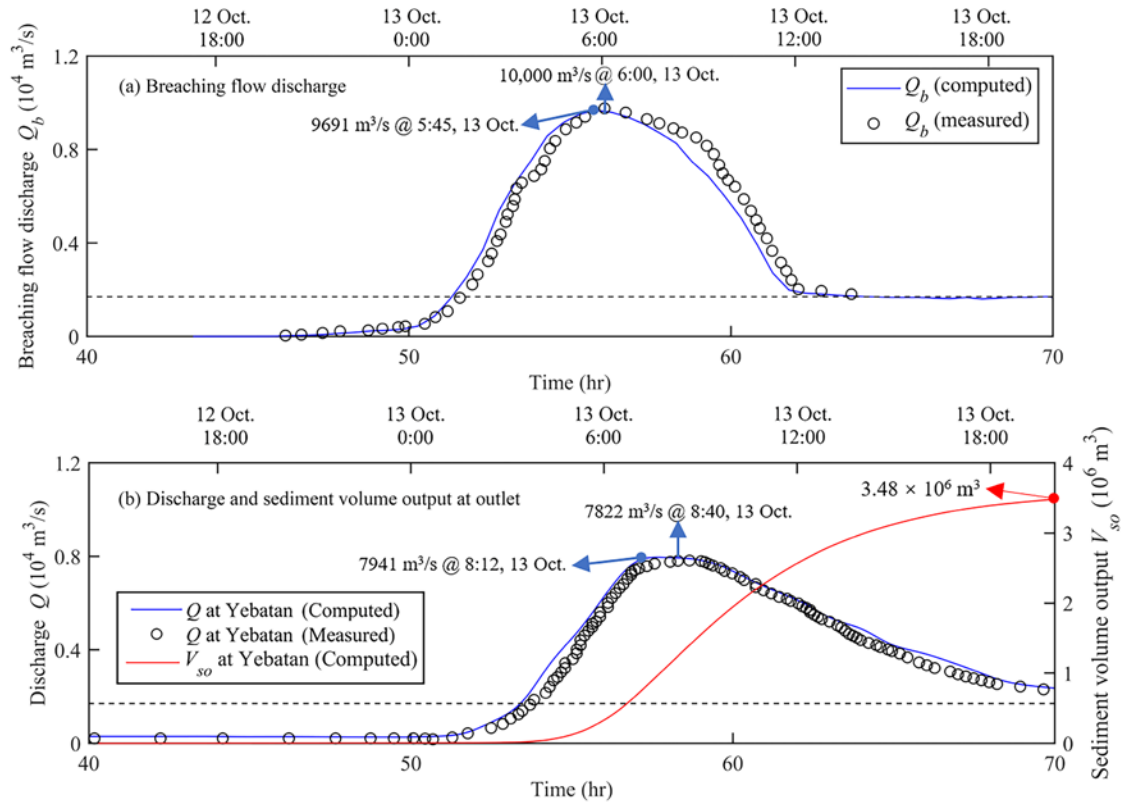
Fig. 8. (a) Breaching flow discharge hydrograph and (b) flow discharge hydrograph and sediment volume output time series at the Yabatan gauging station: model predictions (solid lines) and measured data from Cai et al. (2019) (open black circles).

Fig. 9. Water level time series at the barrier lake and selected sites downstream of the "10.10" Baige landslide dam.

Fig. 10 presents contour plots of the water depth, sediment layer thickness, and changes to bed elevation at different times throughout the barrier lake outburst and subsequent flood processes. Once the barrier lake fills with upstream river inflow, the lake's water level exceeds the crest of the dam and overtopping begins (Fig. 10a1, $t =$ 43 hr at 17: 00 on 12 October), and the landslide dam body is slightly eroded (Fig. 10c1). The predicted time of first overtopping is half-hour earlier than measured. Five hours after overtopping commences ($t =$ 48 hr at 22: 00 on 12 October), the breaching flow reaches Yebatan and the Jinsha river

468   downstream of the landslide dam resumes flowing with a rather low discharge (Fig. 10a2).

469   Meanwhile, the overtopping flow gradually erodes the downstream face of the landslide dam

470   (Fig. 10c2). Subsequently, the overtopping flow rapidly increases (Fig. 8), attaining a value

471   almost equal to the upstream inflow discharge by $t = $ 51 hr at 01: 00 on 13 October and

472   peaking at $t = $ 55.75 hr at 05: 45 on 13 October. During this stage, the water depth

473   downstream of the landslide dam significantly increases, while its upstream counterpart

474   accordingly decreases (Fig. 10(a3-a4)). Within a further two and half hours, the peak

475   discharge arrives at Yebatan (Fig. 10a5). Meanwhile the landslide dam is eroded remarkably,

476   leading to a significant decrease in its crest elevation (Fig. 10(c3-c5)). After time $t = 64$ hr at

477   14: 00 on 13 October, a new river channel forms and the Jinsha river resumes base flow, and

478   is unable to erode further the landslide dam, thus terminating the dam breach process (Fig.

479   10(a6, b6 and c6)).

480
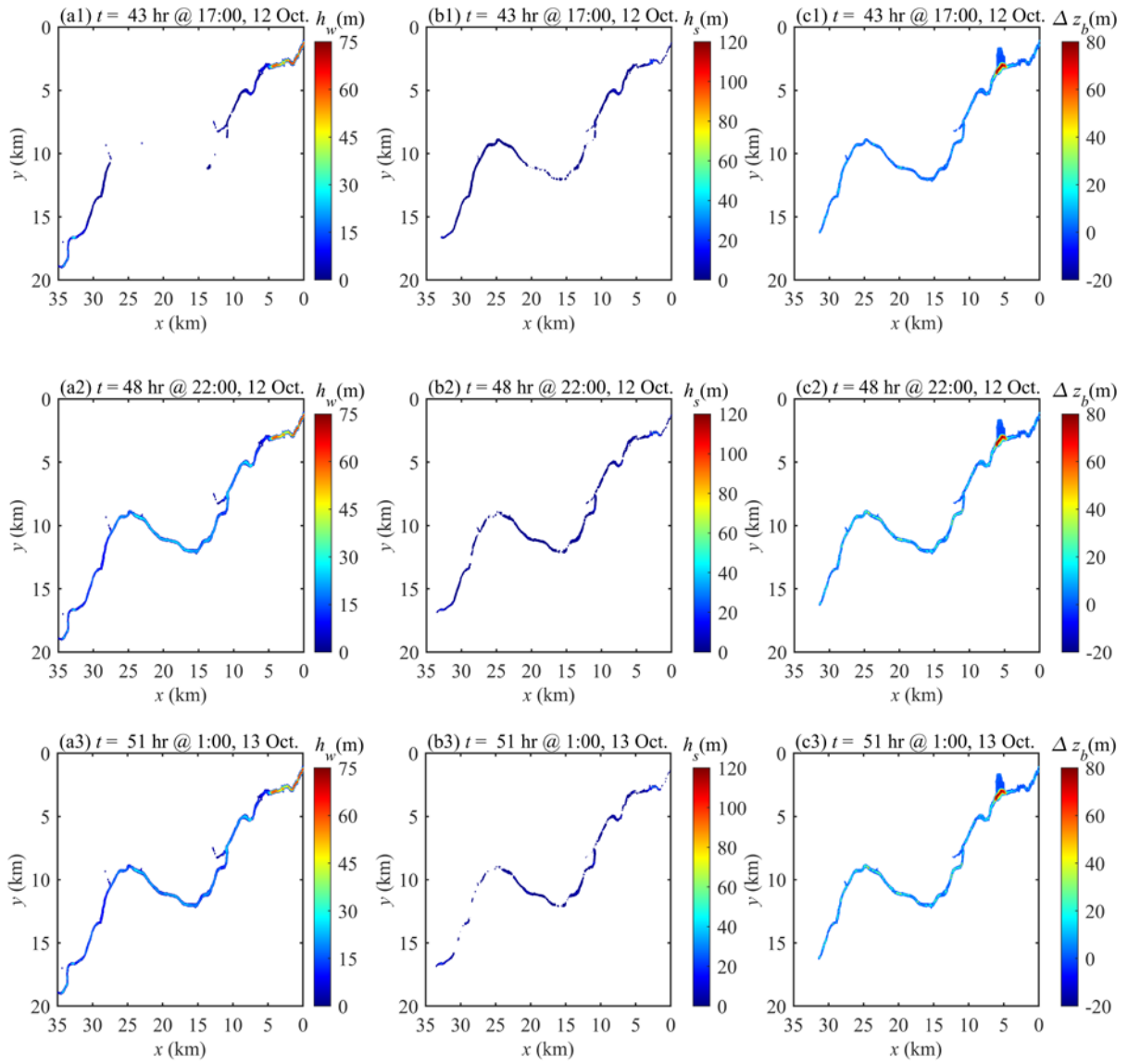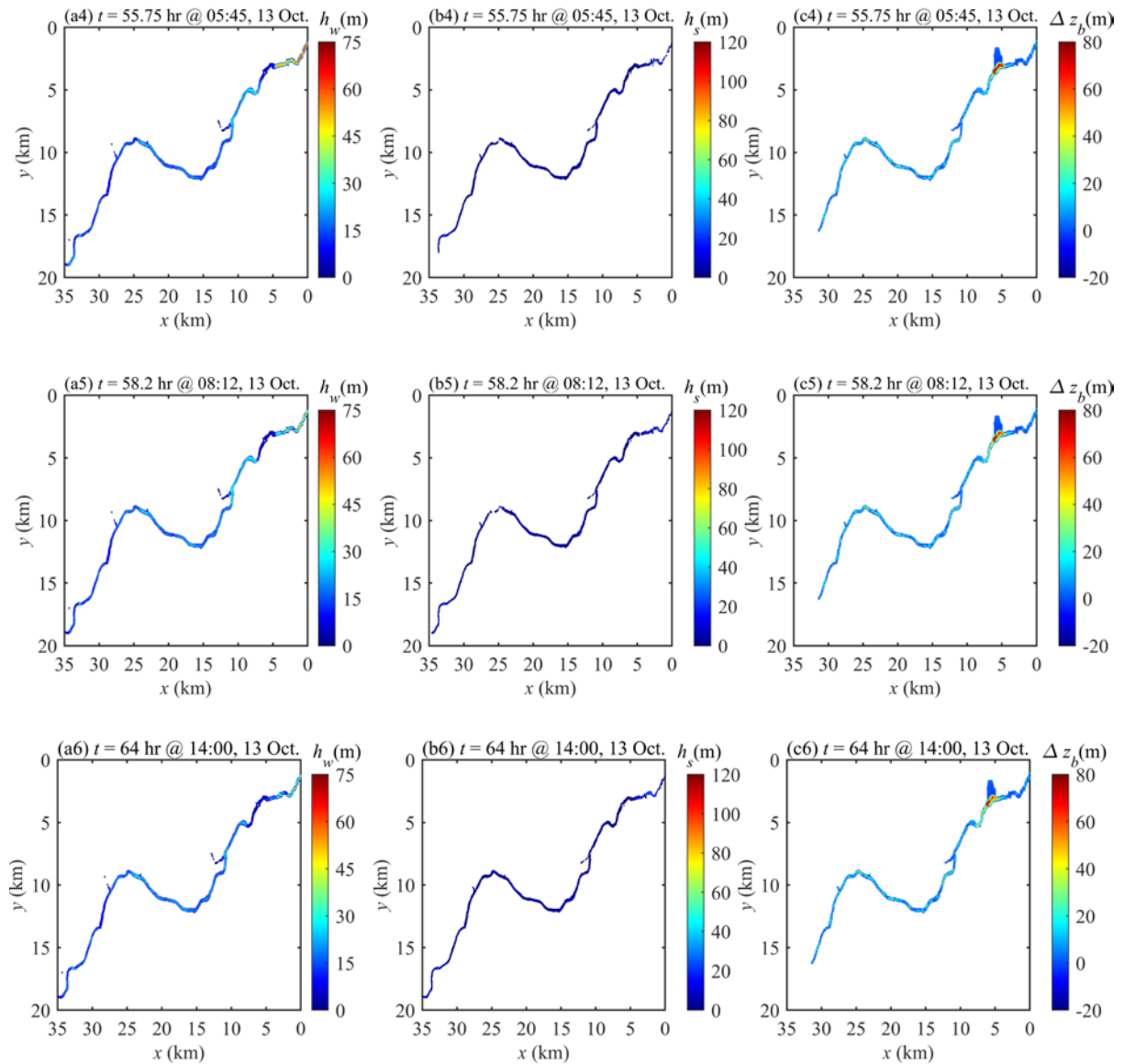
481

Fig. 10. "10.10" Landslide-induced barrier lake outburst and the resultant flood: (a1-a6) depth of water layer; (b1-b6) water-sediment mixture thickness; and (c1-c6) bed deformation. (a1, b1 and c1) Landslide dam is overtopped naturally and dam breach commences. (a2, b2 and c2) Breaching flow arrives at Yebatan. (a3, b3 and c3) Breaching flow discharge is almost equivalent to upstream inflow discharge. (a4, b4 and c4) Breaching flow peaks. (a5, b5 and c5) Peak breaching flow arrives at Yebatan. (a6, b6 and c6) Jinsha river resumes its base flow and the dam breach process terminates.

492   *4.1.4 Interphase interactions*

493   Interphase interactions are evaluated by means of relative velocities. Physically,

494   interphase interactions quantify momentum and energy transfers between grains and fluid

495   (Shan and Zhao, 2014), and hence characterize wave hydrodynamics and sediment transport

496   arising from granular landslides impacting water bodies (Zitti et al., 2016; Miller et al., 2017).

497   Based on laboratory-scale case studies, Li et al. (2020) revealed that grains play a key role in

498   driving water movement during the formation of a landslide dam and its associated barrier

499   lake. However, the subsequent dam breaching process has not yet been fully resolved. Here

500   U_{fs} and V_{fs} are defined as longitudinal (x–axis) and transverse (y–axis) velocity

501   differences between the water phase of the water-sediment mixture flow layer and the

502   sediment phase of a given size Accordingly, $U_{fs}=u_f-u_{sk}$ and $V_{fs}=v_f-v_{sk}$, where u_f

503   and v_f are the layer-averaged velocity components of the water phase in the water-sediment

504   mixture flow layer; and u_{sk} and v_{sk} are the size-specific layer-averaged velocity

505   components of the sediment phase in the water-sediment mixture flow layer. Fig. 11 displays

506   the velocity differences between the water and size-specific sediment phases in the transverse

507   direction, and Fig. 12 shows their counterparts in the longitudinal direction. Specifically, Figs.

508   11 (a1-a3 and b1-b3) and Fig. 12 (a1-a3 and b1-b3) depict the barrier lake formation process,

509   whereas the remaining subplots refer to the barrier lake outburst and subsequent flood.
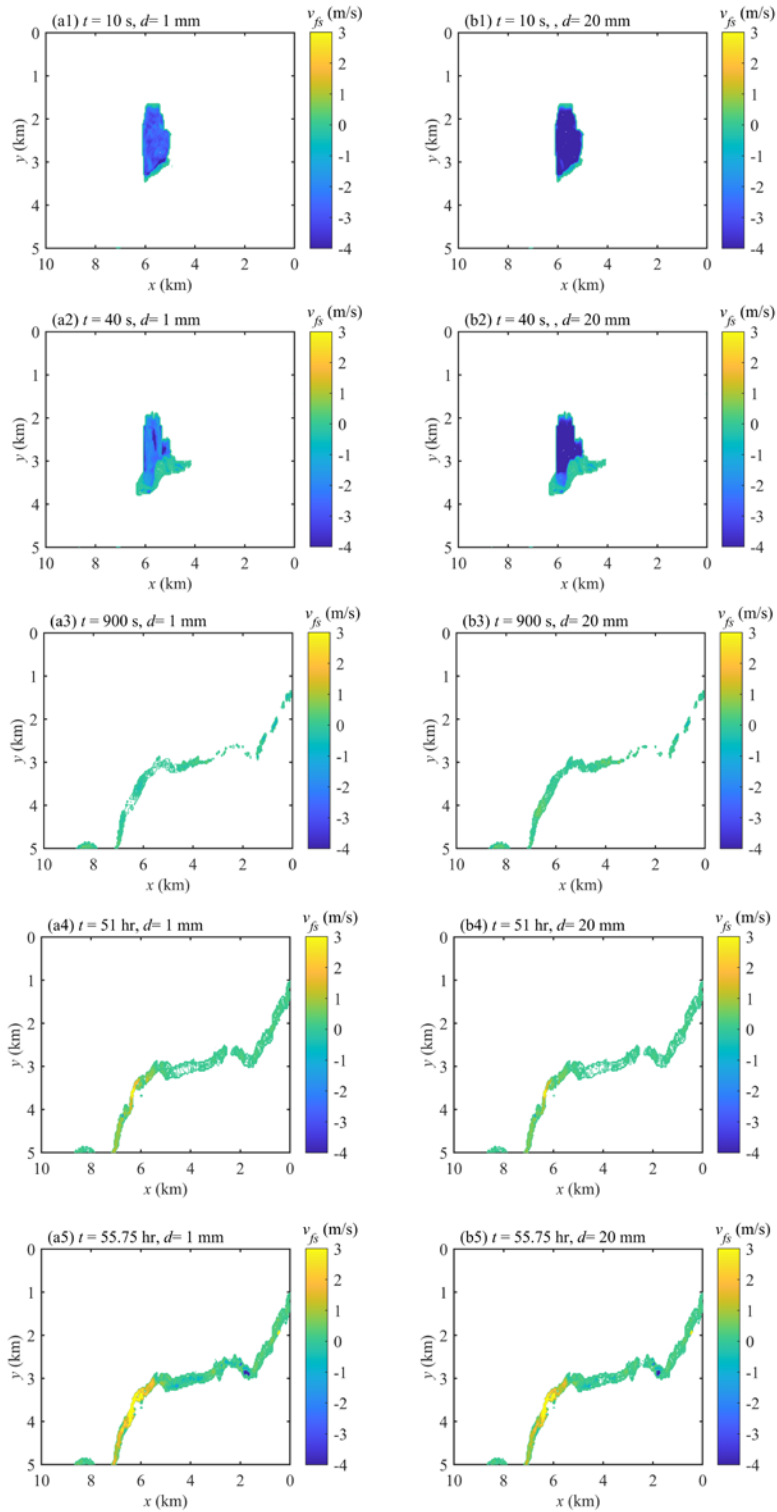
510   During barrier lake formation, as seen in Figs. 11 (a1-a3 and b1-b3) and Figs. 12 (a1-a3

511   and b1-b3), sediment grains play a primary role in driving water movement, echoing the

512   finding from a laboratory-scale study by Li et al. (2020). Specifically, the grains generally

513   have higher speed than the water phase in both the transverse and longitudinal directions.

514   Comparatively, the magnitude of velocity difference in the transverse direction (V_{fs}) is

515   significantly greater than that in the longitudinal direction (U_{fs}). Furthermore, coarse grains

516   move approximately 30% - 40% faster than fine grains in the transverse direction (Fig.

517   11(a1-a2)), whereas the velocity difference shrinks to 10%-20% in the longitudinal direction

518   (Fig. 12(a1-a2)). By $t =$ 900 s, as a landslide dam forms due to material deposition, the

519   velocity differences between the water and sediment phases almost vanish.

520   By contrast, the reverse behaviour occurs during the succeeding processes, as water

521   governs grain movement. Figs. 11 (a4-a5 and b4-b5) and Figs. 12 (a4-a5 and b4-b5) show

522   that the water phase generally exhibits higher speed than the grains, and that fine grains move

523   faster than coarse grains. Although measured data are unavailable to verify quantitatively the

524   computed results, the present finding is qualitatively consistent with existing experimental

525   fluvial process observations (Wilcock, 1997) and field data (Drake et al., 1988; Ferguson and

526   Wathen, 1998; Lenzi, 2004); this further demonstrates the satisfactory performance of the

527   present model.

528   Figs. 11 and 12 collectively show that water and grain velocities are distinct, thus

529   characterizing the primary role of grains in driving water movement during landslide dam

530   and barrier lake formation and the governing role of water in driving grain movement during

531   barrier lake outburst and the subsequent flood. Overall, these results imply that a double

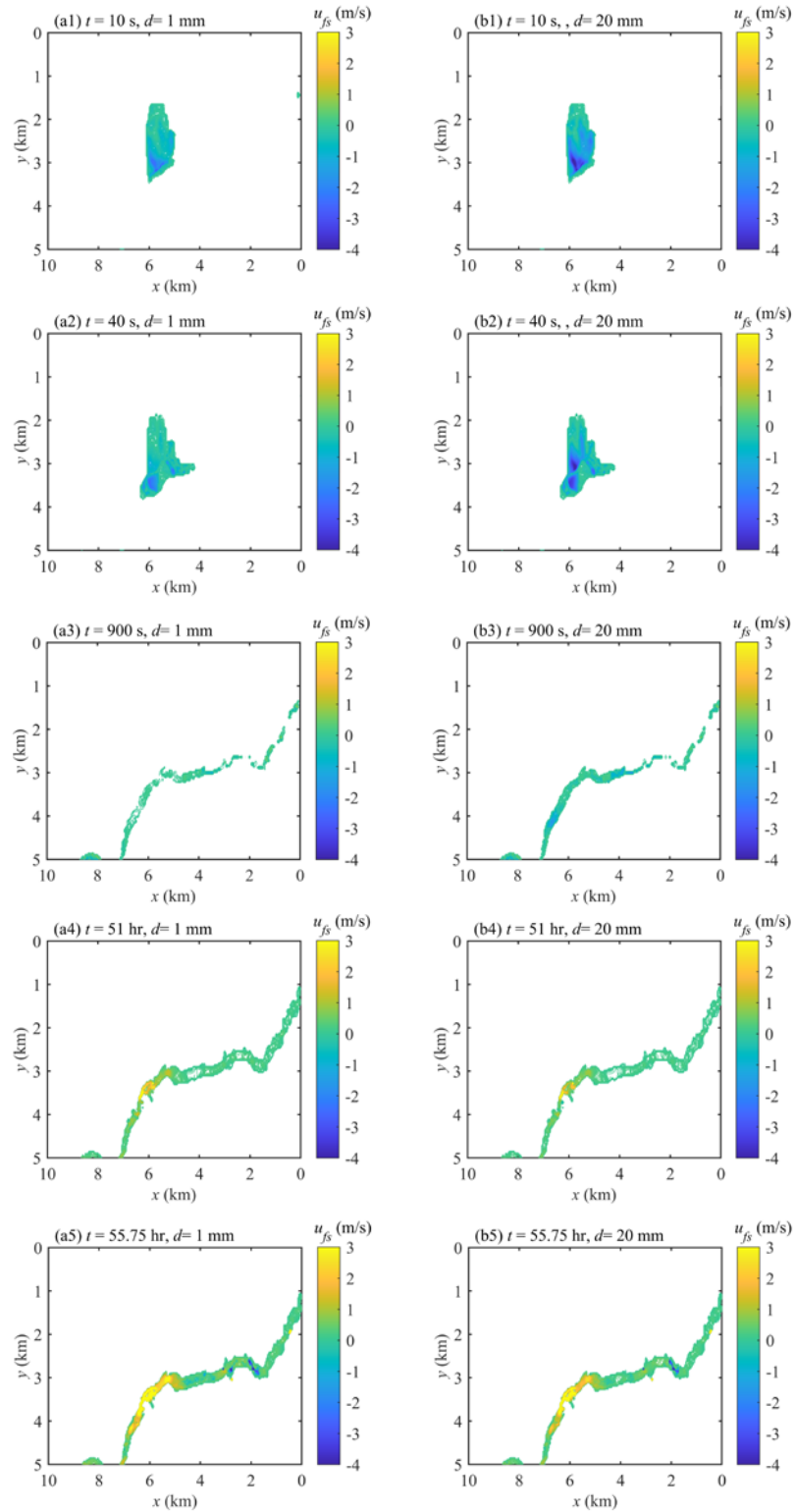532   layer-averaged two-phase flow model is warranted.

533

Fig. 11. Contour plots of velocity difference between water and sediment phases of the water-sediment mixture flow layer in the transverse ($y-$ axis) direction at different times from 10 s to 55.75 hr after the start of the "10.10" Baige landslide: a1–a5 with $d=1$ mm; and b1–b5 with $d=20$ mm.

540

Fig. 12. Contour plots of velocity difference between water and sediment phases of the
water-sediment mixture flow layer in the longitudinal (x – axis) direction at different times
from 10 s to 55.75 hr after the start of the "10.10" Baige landslide, a1-a5 with $d = 1$ mm,
and b1-b5 with $d = 20$ mm.

545

4.1.5. Effects of inflow discharge and landslide volume

Laboratory-scale case studies have found that smaller river flow discharge and larger landslide volume favour landslide dam and barrier lake formation (Li et al., 2020). Here, two series of extended numerical cases, designed according to the Phase I "10.10" Baige barrier lake event, are used to investigate the effects of inflow discharge and landslide volume on a landslide-induced multi-hazard chain. This is sensible given that potentially unstable rock mass clusters have been discovered in the source area of the Baige landslides, suggesting possible future failures with the potential for river damming and flooding (Fan et al. 2020a).

4.1.5.1. Inflow discharge (Series 1 tests)

Runoff variations in the upper tributaries of the Jinsha River are vulnerable to climate change (Wu et al., 2020). It is therefore useful to explore the impacts of different upstream inflow discharges on the landslide-induced multi-hazard chain. Here, the inflow discharge is tuned by 25% (i.e., 1680 ± 420 m^3/s), and the corresponding results are displayed in Table 3 and Fig. 13. As the inflow discharge increases, the time taken to form a landslide dam increases and the dam height decreases. This is consistent with the observation by Li et al. (2020) that small river discharge is conducive to barrier lake formation. In the present simulations, the time taken to overtop the dam drops substantially from 50.3 hr to 43 hr, and further to 36.5 hr, as the inflow discharge increases from 1260 m^3/s to 1680 m^3/s, and further to 2100 m^3/s. From these, corresponding marked reductions in the time available to evacuate downstream residents may be inferred. Therefore, the risk arising from a barrier lake outburst would be significantly amplified if the barrier lake was created in the rainy season. The

567 simulations also indicate that after the dam overtops naturally, the subsequent peak breach

568 flow discharge increases for higher inflow discharge (Table 3 and Fig. 13). Consequently, the

569 larger the inflow discharge, the more rapidly the dam is eroded and the shorter the total

570 breach duration.

571

572 **Table 3** Predicted effect of inflow discharge on landslide dam formation, overtopping, and
573 breaching processes (Series 1 tests)

Results	"10.10" Baige landslide	Series 1-1	Series 1-2
	Q_{inflow}	Q_{inflow}	Q_{inflow}
	(m^3/s)	(m^3/s)	(m^3/s)
	1680	2100	1260
Time to form landslide dam (s)	900	1230	765
Maximum dam height (m)	84.2	76.5	87.2
Time to overtop dam (hr)	43	36.5	50.2
Total breach duration (hr)	21	18.5	23
Peak discharge at dam site (m^3/s)	9691	10006	8724

574
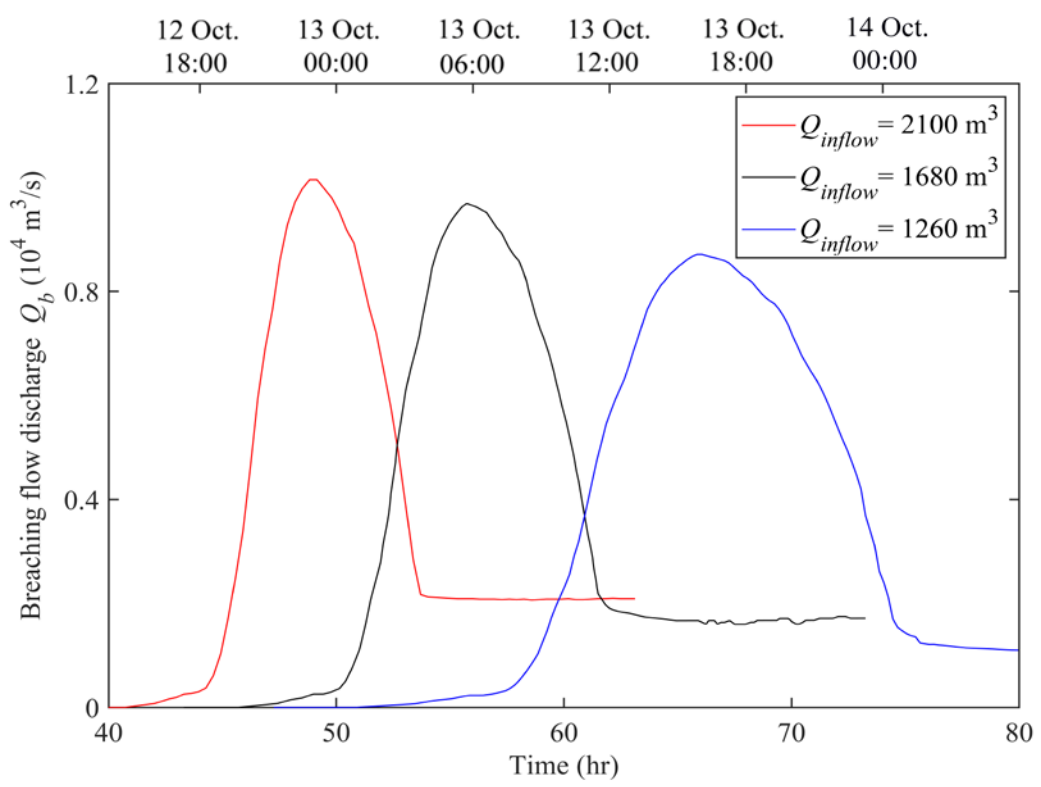
575

576 **Fig. 13.** Model predictions of breaching flow discharge hydrographs for three different Jinsha

577 river inflow discharges.

578

579 *4.1.5.2. Initial landslide volume (Series 2 tests)*

580   For landslide-induced risk assessment, it is of great importance to obtain a measure of the

581 landslide magnitude, e.g., through estimating the volume of landslide materials involved

582 (Corominas et al., 2014; Fan et al., 2020b). Although the position and movement of a

583 landslide can be successfully captured by advanced techniques like remote sensing (Zhang et

584 al., 2020), quantification of the initial volume of a landslide nevertheless involves

585 considerable uncertainty. With this in mind, Series 2 simulations have been undertaken to

586 investigate the sensitivity of the results to the initial landslide volume, which is altered by

587 ±50% of the original volume of $27.5 \times 10^6 \, \text{m}^3$. Table 4 summarizes the results from the Series

588 2 simulations, whereas Fig. 14 displays the breaching flow hydrograph under different initial

589 landslide volumes. In accordance with Li et al. (2020), a larger initial landslide volume

590 favours barrier lake formation as the time to form a landslide dam decreases and the

591 maximum dam height increases. Hence, the time taken to overtop the dam increases as the

592 initial landslide volume increases. Subsequently, the breaching process is postponed and the

593 total breach duration extended. Yet, the peak discharge at the dam site just slightly increases.

594

595 **Table 4** Predicted effect of inflow landslide volume on landslide dam formation, overtopping,
596 and breaching processes (Series 2 tests)

Results	"10.10" Baige landslide	Series 2-1	Series 2-2
	V_0	V_0	V_0

	(10^6 m^3)	(10^6 m^3)	(10^6 m^3)
	27.5	41.25	13.75
Time to form landslide dam (s)	900	700	1356
Maximum dam height (m)	84.2	90.2	74.5
Time to overtop dam (hr)	43	45.3	40.5
Total breach duration (hr)	21	23.7	16.5
Peak discharge at dam site (m^3/s)	9691	9845	9170

597
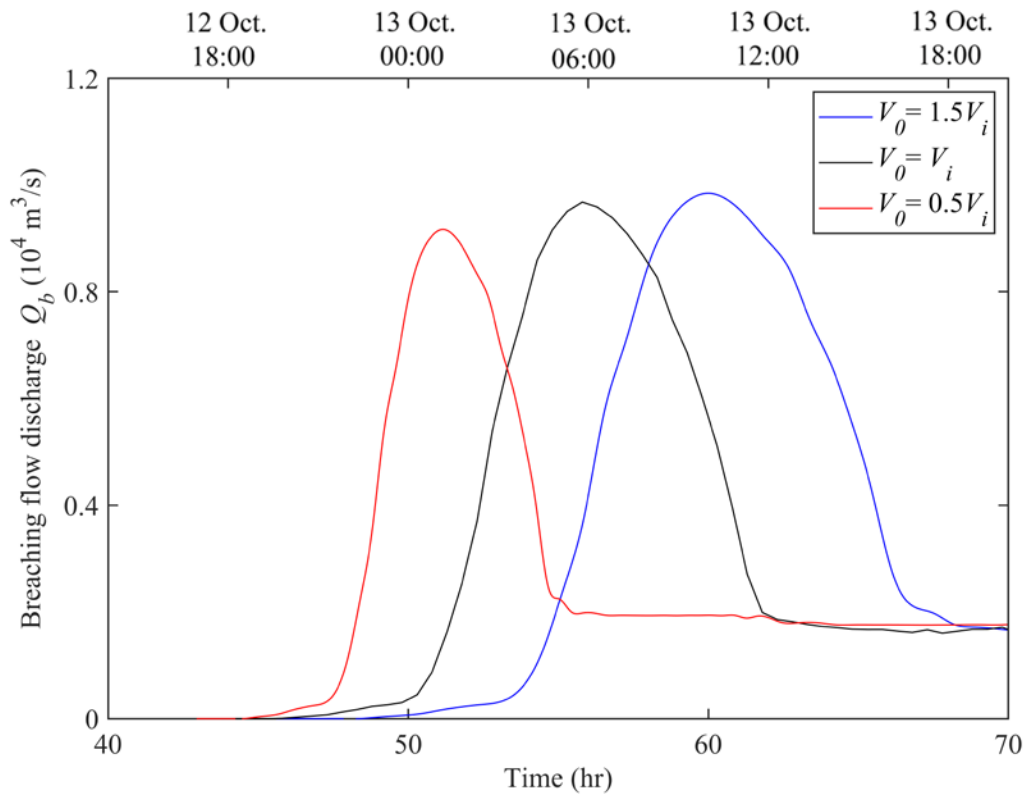
598

Fig. 14. Model predictions of breaching flow discharge hydrographs for three different initial landslide volumes.

601

The above analysis clearly demonstrates that whereas small inflow discharge and large initial landslide volume favour landslide dam and barrier lake formation, they delay the subsequent barrier lake outburst and the resultant flood downstream. From a physical perspective, the formation of a landslide dam and its associated barrier lake generally reflects an aggradation process, whereas the barrier lake outburst and subsequent flood are

39

607 characterized by an opposing degradation process. The present model properly

608 accommodates these two distinct but intertwined physical processes, thus facilitating

609 improved understanding of the complicated physical mechanisms leading to a

610 landslide-induced barrier lake outburst flood as a multi-hazard causal chain.
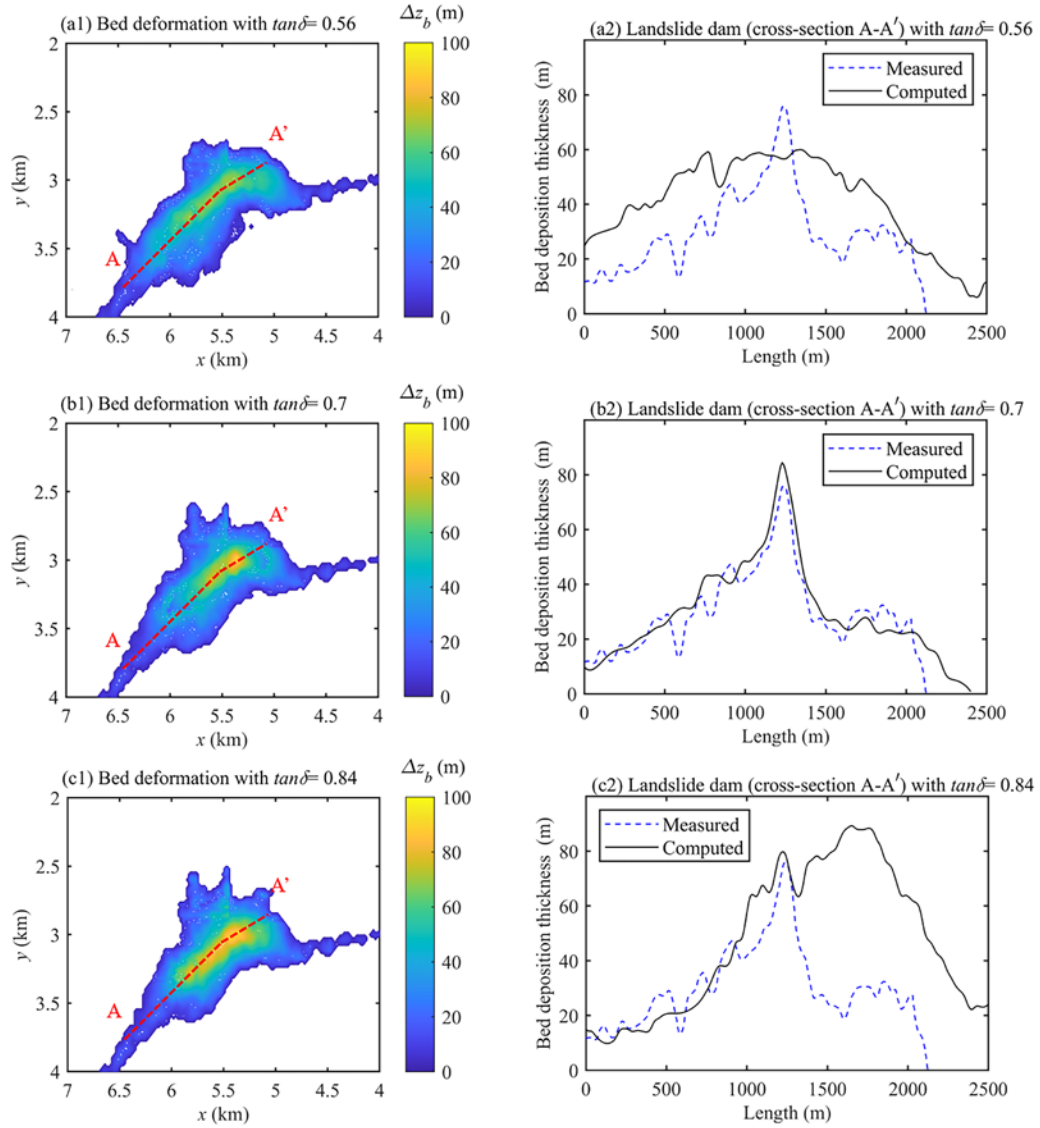
611

4.1.6 Sensitivity analysis

613 Furthermore, numerical tests are conducted to evaluate the sensitivity of the model

614 results to two model parameters, i.e., bed friction coefficient $\tan\delta$ and Manning bed

615 roughness coefficient n_b, which are separately embedded in the empirical relationships for

616 the solid and fluid resistance components of the lower sediment-laden flow layer. In addition,

617 the Manning bed roughness coefficient n_b is also involved in the bottom resistance of the

618 clear-water flow layer (Li et al., 2020). Specifically, the Manning bed roughness coefficient

619 n_b and the bed friction coefficient $\tan\delta$ are tuned by 25% of the adopted value (i.e.,

620 $n_b = 0.04 \pm 0.01$ m$^{-1/3}$ s; $\tan\delta = 0.7 \pm 0.14$). In general, the results with tuned parameters in

621 conventional ranges are qualitatively similar to those shown above when compared with the

622 measured data.

623 Shown in Figs. 15 and 16 are the computed landslide dam morphology, corresponding to

624 different values of n_b and $\tan\delta$. Clearly, the computed results are more sensitive to the

625 value of bed friction coefficient $\tan\delta$ as compared to that of Manning bed roughness

626 coefficient n_b. Most notably, the sensitivity to n_b is considerably constrained compared

627 with that to $\tan\delta$. Typically, as the value of $\tan\delta$ increase from 0.56 to 0.84, the value of

628   maximum dam height increases from 59.2 m to 89.5 m. By contrast, in response to the

629   change of n_b, their counterparts almost remain unchanged. This difference in behavior

630   further demonstrates the primary role of grains in driving water movement during landslide

631   dam and barrier lake formation.

632   Fig. 17(a) shows the impact of $\tan\delta$ on breaching flow discharge. As shown in Fig. 15,

633   a larger value of $\tan\delta$ leads to a higher maximum dam height. Consequently, the time taken

634   to overtop the dam increases and the subsequent breaching process is postponed. These

635   simulations also indicate that the peak breaching flow discharge increases for a larger value

636   of $\tan\delta$. Specifically, with $\tan\delta = 0.56$, the peak discharge is 8732 m³/s occurring at $t =$

637   49.6 hr, whereas with $\tan\delta = 0.84$, the peak discharge increases to 10170 m³/s, postponing to

638     $t = $ 61.88 hr. Fig. 17(b) illustrates the effect of n_b. Despite its marginal impact on landslide

639   dam morphology, a larger value of n_b leads to a larger peak discharge and an earlier

640   occurrence. Specifically, with n_b increasing from 0.03 to 0.05 m⁻¹ᐟ³ s, the peak discharge

641   increases from 8700 m³/s to 10400 m³/s and its timing is advanced from $t = $ 61.3 hr to $t =$
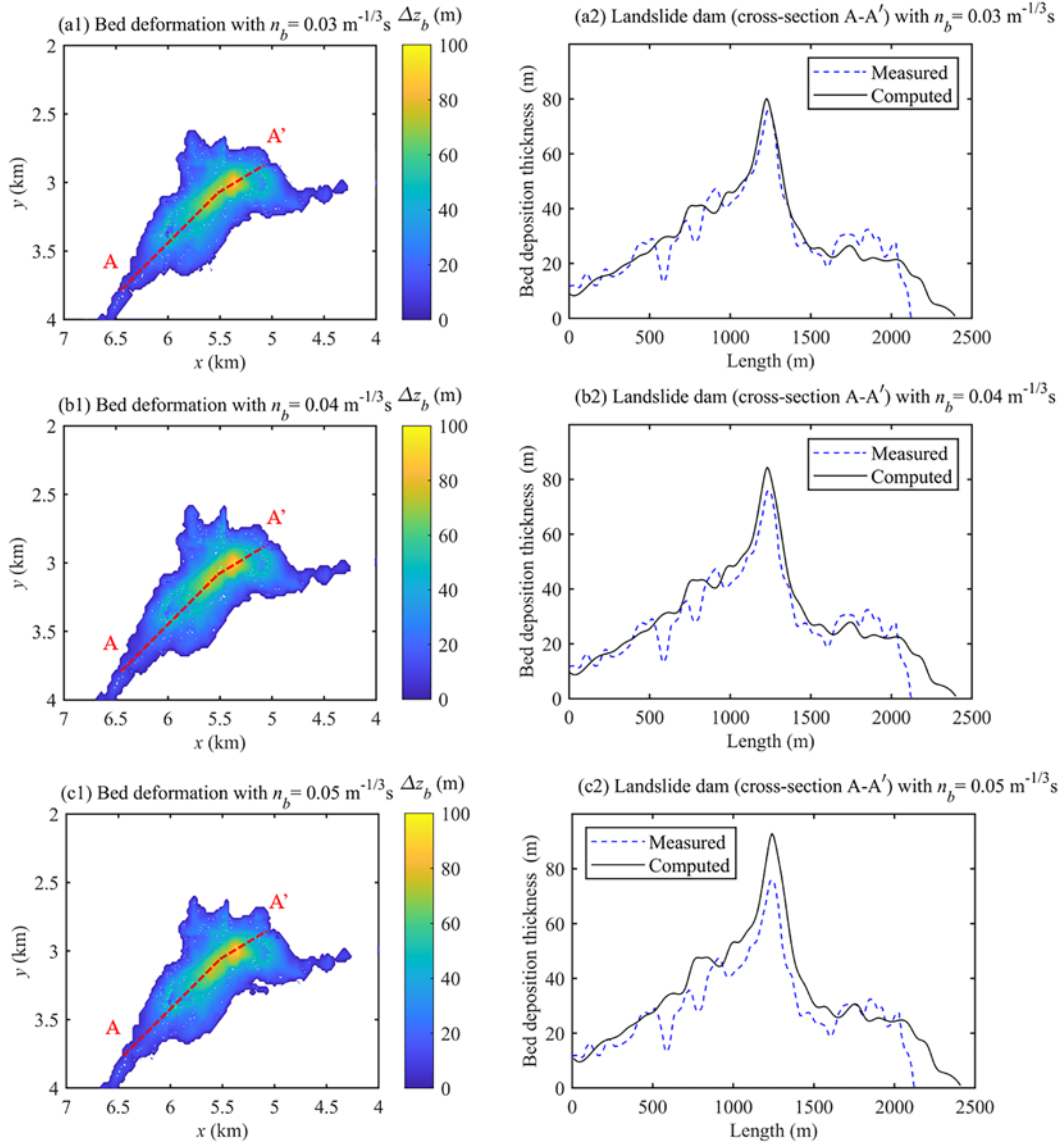
642   51.6 hr.

643

Fig. 15. "10.10" Baige landslide dam morphology assuming different bed friction coefficient $\tan\delta$ (a1-a3) bed deform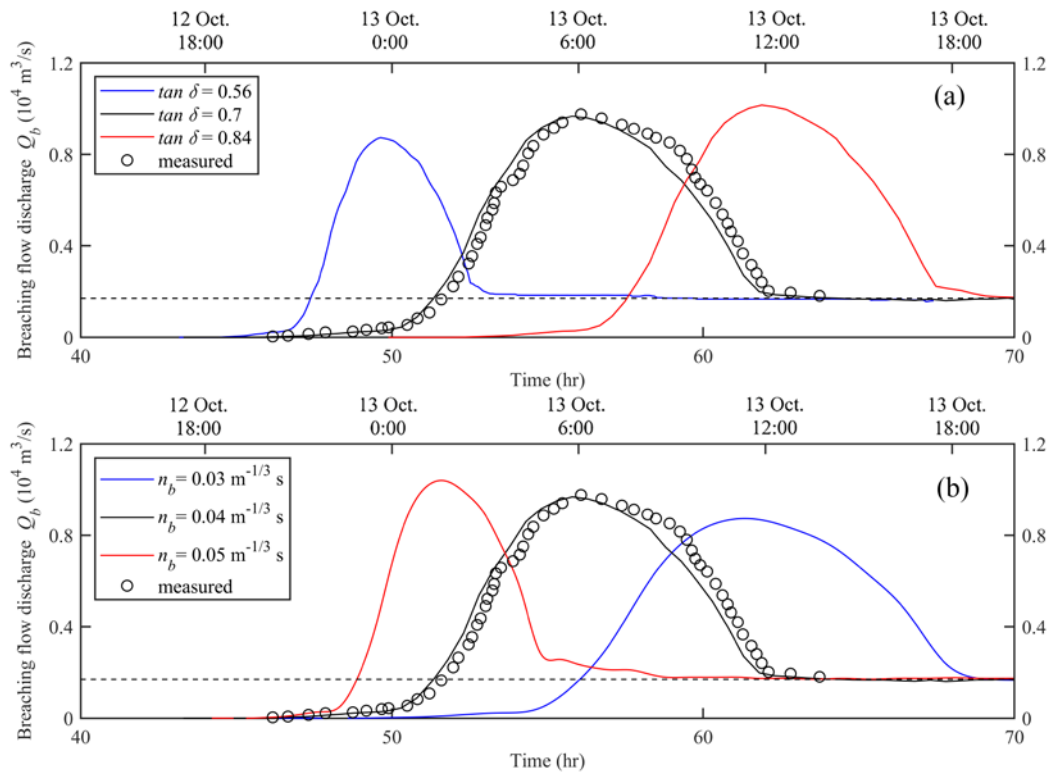ation at $t = 900$ s predicted by present model; and (b1-b3) cross-section profile of landslide dam in the original river stream-wise direction (A-A'): model prediction (solid line) and measured data from Fan et al. (2020a) (dashed line).

Fig. 16. "10.10" Baige landslide dam morphology assuming different Manning roughness

coefficient n_b (a1-a3) bed deformation at $t =$ 900 s predicted by present model; and

(b1-b3) cross-section profile of landslide dam in the original river stream-wise direction

(A-A'): model prediction (solid line) and measured data from Fan et al. (2020a) (dashed line).

Fig. 17. Model predictions (solid lines) of breaching flow discharge hydrographs assuming (a) different bed friction coefficient $\tan\delta$; and (b) different Manning roughness coefficient n_b and measured data (open circles) from Cai et al. (2019).

4.2. Phase II: "11.03" Baige barrier lake event

We now revisit the Phase II "11.03" Baige barrier lake event. This second landslide dam formed on residual material from the first landslide dam, causing the barrier lake to triple in volume. To reduce downstream flood risk due to barrier lake outburst, an artificial flood channel was urgently constructed, with a total of 85,000 m³ of soil and rock excavated (Cai et al., 2019).

Fig. 18(a) shows the landslide dam morphology as represented by the bed deformation at $t = 900$ s (noting that $t = 0$ s is now set to the start of the "11.03" landslide). Similar to its predecessor due to the first landslide (Fig. 6), the height of the second landslide dam is higher on the upstream relative to the downstream side with respect to the Jinsha river. Fig. 18(b)

44

presents predicted and observed cross-section profiles of the landslide dam taken in a

longitudinal direction approximately along the river (B-B', see Fig. 18a). The L^1 norm for

bed deposition thickness L^1_{bd} = 22.38%. The present model predictions are in reasonable

agreement with observed data, except for a general overprediction of the bed deposition layer

thickness.

Fig. 19 presents discharge hydrographs and water level time series at the landslide dam

site and the Yebatan station. Although quantitative differences between the model predictions

and field observations are inevitable, the computed discharges and water levels are reasonably

consistent with those reported by Cai et al. (2019). The model predicts a peak breach

discharge of 32,787 m³/s, occurring at 17:28 on 13 November, a difference in maximum

discharge of 3.2% and occurrence time of < 1 hr compared to the observed data. The

predicted water level time history at the dam site is remarkably close to the measured series at

Boluo station, 20 km upstream of the dam, until the barrier lake outburst occurs, after which

the predicted result at the dam site is appreciably lower than that measured at Boluo. This

behaviour arises because the water level at the Baige landslide dam site was almost

equivalent to that at Boluo while the barrier lake is full, but was appreciably lower than that

at Boluo after the barrier lake outburst occurred. Fig. 19(b) compares predicted and measured

discharge hydrographs at Yebatan, the downstream station, along with computed sediment

volume output time series. Similar to the results obtained for Phase II (Fig. 8), the peak

discharge attenuates as the wave travels along the river. At Yebatan, the peak discharge is

predicted to occur at 19:10 on 13 November, with a value of 26,817 m³/s, whereas the

observed maximum discharge is 28,057 m³/s at 19:50 on 13 November. Subsequently, the

693   Jinsha river gradually reverts to base flow. The corresponding L^1 norms for breaching flow

694   discharge hydrography $L_{Q_b}^1$ and flow discharge hygrograph at Yebatan gauging station L_Q^1

695   are 23.22% and 25.47% respectively. At the end of "11.03" Baige barrier lake event,

696   approximately 5.96×10^6 m^3 of sediments have been carried away through Yebatan.

697   Consequently, an addition 6.04×10^6 m^3 of sediment [$= 12 \times 10^6$ m^3 (total volume of "11.03"

698   Baige landslide) $- 5.96 \times 10^6$ m^3 (sediment volume output)] has been deposited in the river
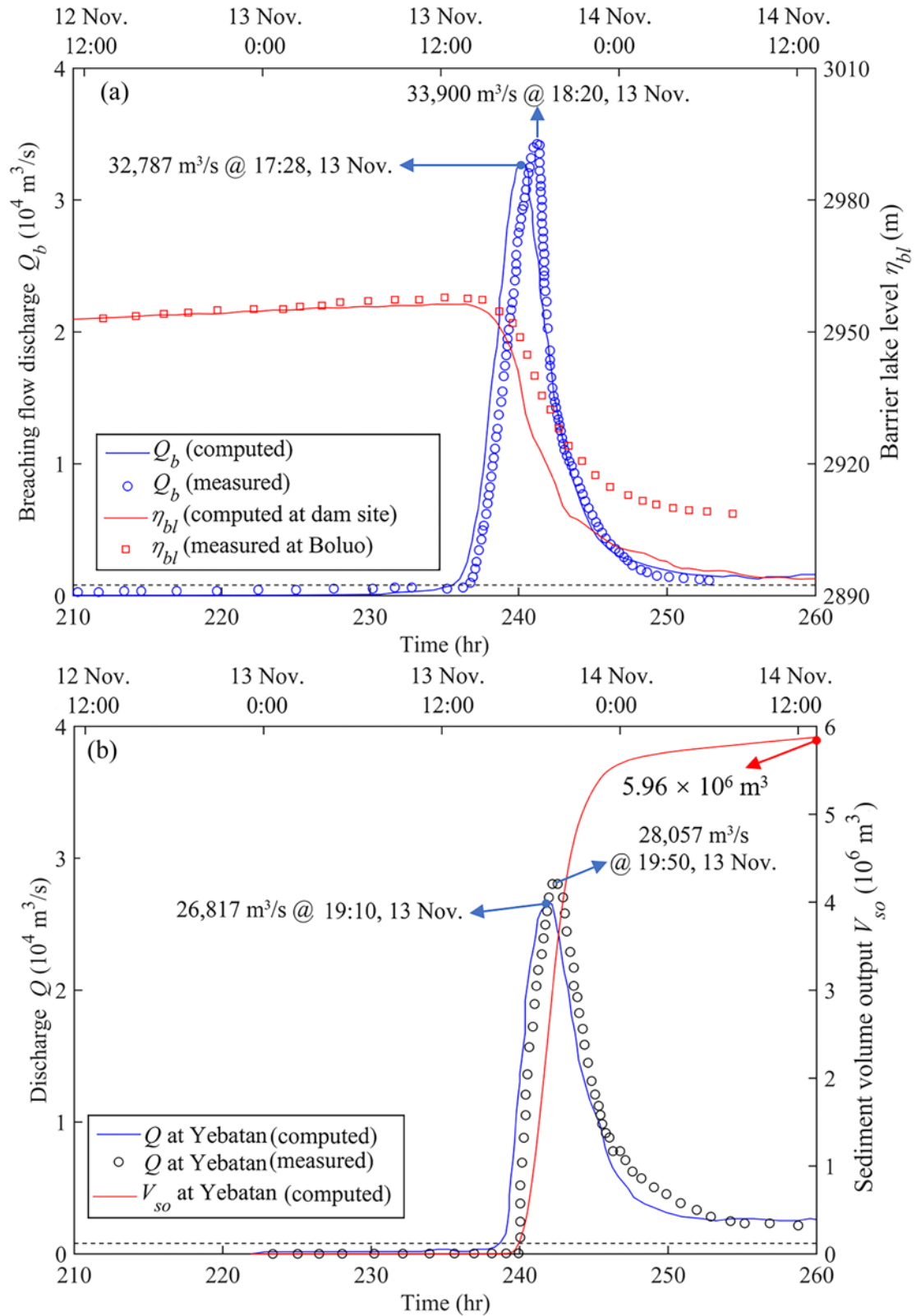
699   channel between dam site and Yebatan.

700
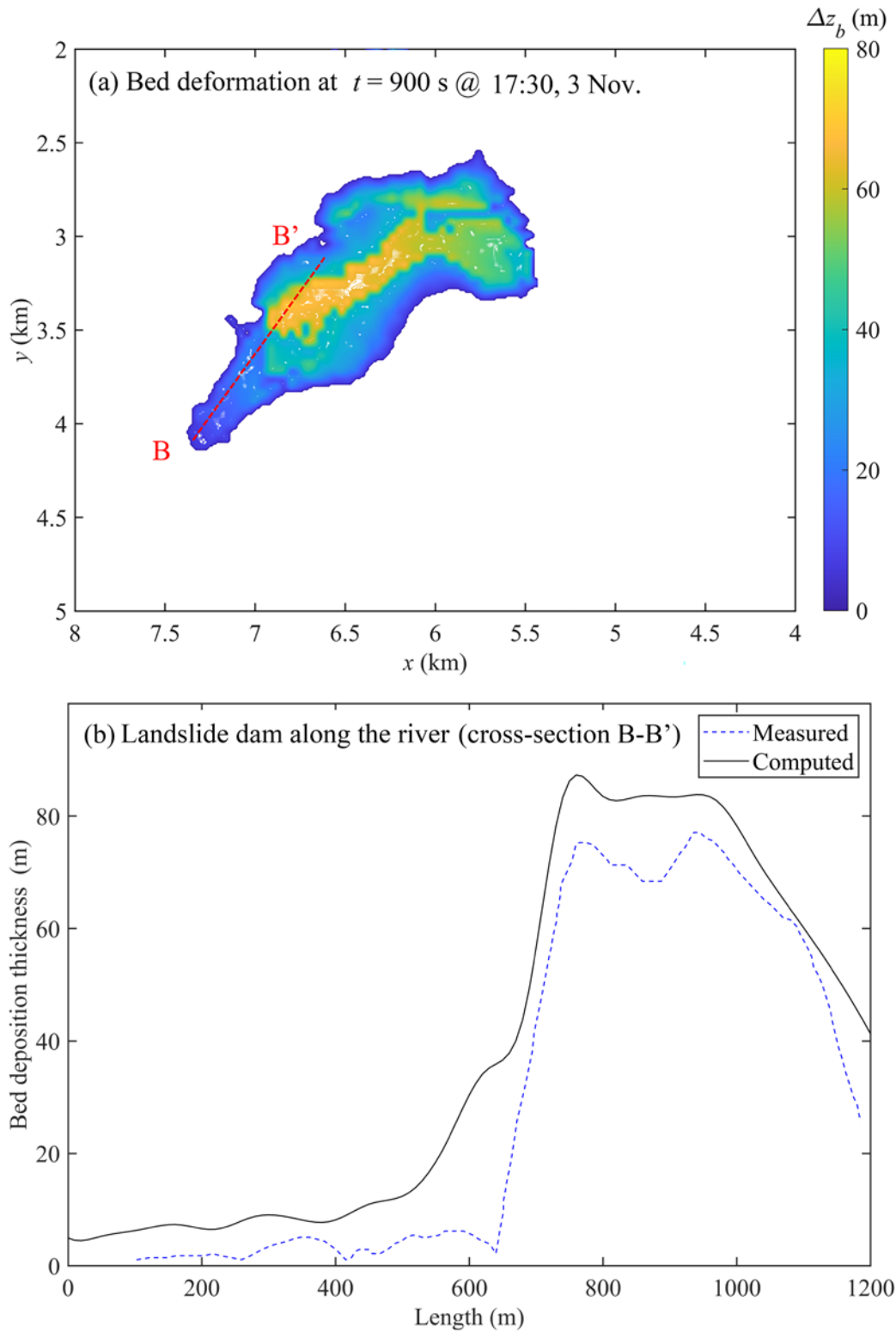
Fig. 18. "11.03" Baige landslide dam geometry: (a) predicted bed deformation contours at $t = 900$ s; and (b) predicted (solid line) and measured (dashed line, Fan et al. 2020a) cross-sectional profiles of the landslide dam in a longitudinal direction along the river (B-B').

Fig. 19. (a) Breaching flow discharge hydrograph and water level time series at the "11.03"
Baige landslide dam site; (b) flow discharge hydrograph and sediment volume output series
at Yebatan (the downstream station): model predictions (solid lines) and measured data (open
circles).

711

712   Fig. 20 presents contour plots of the evolution of the dam breach with instantaneous flow

713 velocity vectors superimposed. At $t =$ 202.75 hr at 4:00 on 12 November (Fig. 20a), the

714 water level of the barrier lake rises above the bed level of the artificial flood channel and

715 overtopping commences. The overtopping flow then traverses the dam crest as an almost

716 uniform sheet. The breach channel hardly widens, while the main dam body slightly erodes

717 (Fig. 20b). During the next stage, breach channel enlarges slowly over a relatively long

718 period (about 24 hrs). Meanwhile, the steepest section of the downstream face of the dam

719 experiences significant erosion (Fig. 20c), which causes the flow velocity to increase locally.

720 The resultant rapid flow in this steep section entrains further sediment and intensive scouring

721 rapidly propagates backward toward the upstream area (Fig. 20d). Such headward erosion

722 raises the breaching flow discharge (Fig. 19), leading to progressive vertical and horizontal

723 enlargement of the breach channel (Fig. 20d and e). In general, breach deepening is

724 associated with steepening of the sidewalls that may collapse once a critical failure angle is

725 exceeded, leading to breach widening. In addition, the river channel downstream of the

726 landslide dam accretes sediment scoured from the dam. The model indicates that high flow

727 speeds, up to 15 m/s occur as the breaching flow discharge increases. Accordingly, both flow

728 speed and bed erosion decrease as the barrier lake water level decreases and the river flow

729 returns to base flow (Fig. 20f).
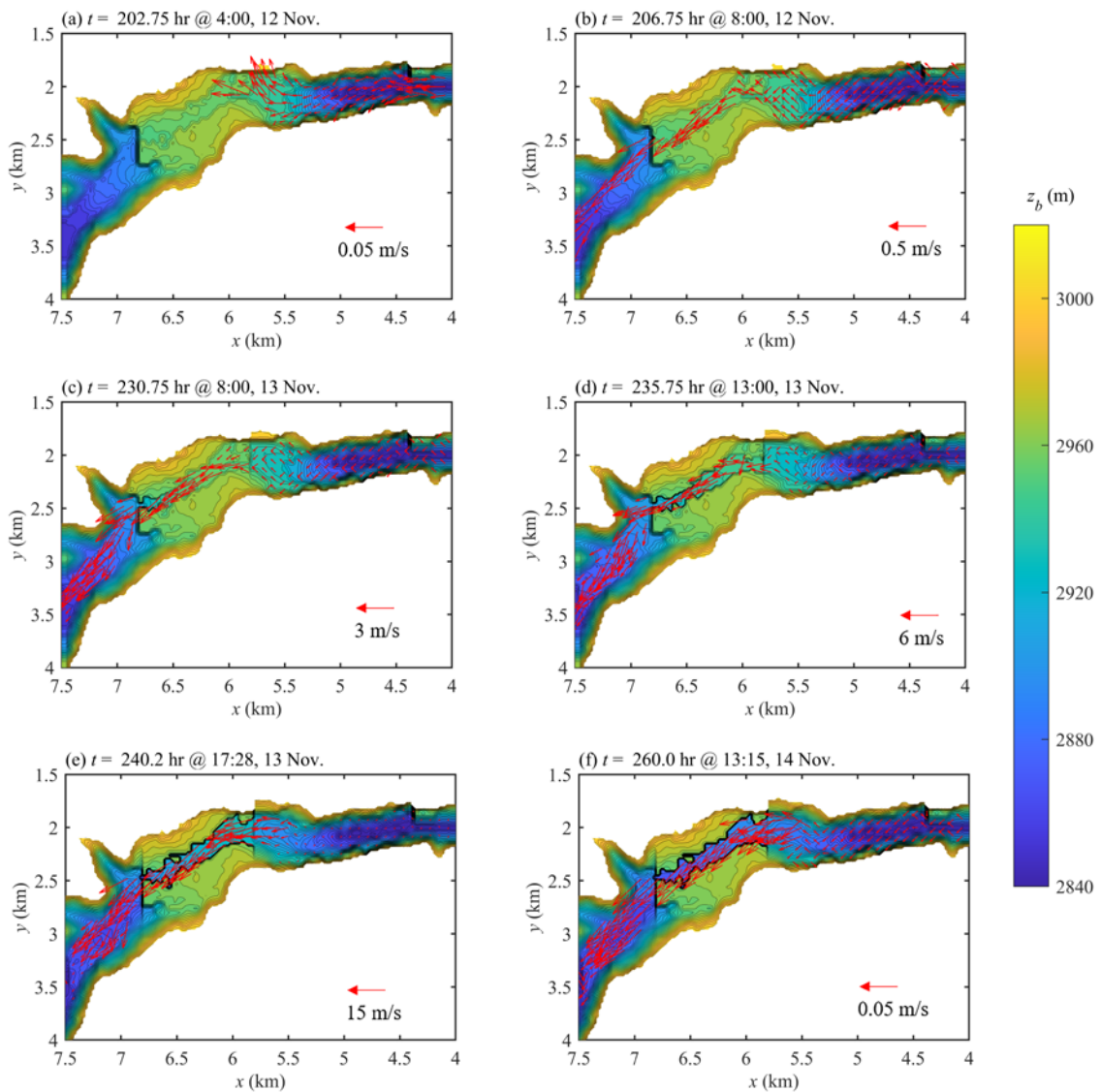
730

Fig. 20. "11.03" Baige landslide dam breach evolution depicted as bed deformation contours and superimposed flow velocity vectors at post-landslide times, $t =$: (a) 202.75 hr; (b) 206.75 hr; (c) 230.75 hr; (d) 235.75 hr; (e) 240.2 hr; and (f) 260.0 hr.

A further scenario is now considered for the case of the second landslide dam in the absence of an artificial flood channel. The computation automatically terminated once the river flow returned to base flow. Fig. 21 displays the predicted breach flow discharge hydrograph and barrier lake level time series. In the absence of an artificial flood channel, the

50

740 breaching process is significantly delayed, the peak discharge much larger, and the barrier

741 lake level raised. This finding is qualitatively consistent with experimental observations from

742 another landslide dam failure (Cao et al., 2011a). For a constant inflow discharge of 800 m^3/s,

743 the model estimates that 3 more days will be taken to fill the barrier lake and overtop the

744 landslide dam (than for the case with the artificial channel present). In the absence of the

745 channel, the model predicts that the peak breaching flow discharge would reach 51,884 m^3/s

746 (an increase of 58.2%) at 22:45 on 16 November, and the maximum water level of the barrier

747 lake would attain 2967.5 m (an increase of 11.2 m). As would be expected, the model predicts

748 that construction of an artificial flood channel would significantly alleviate downstream flood

749 risk.

750
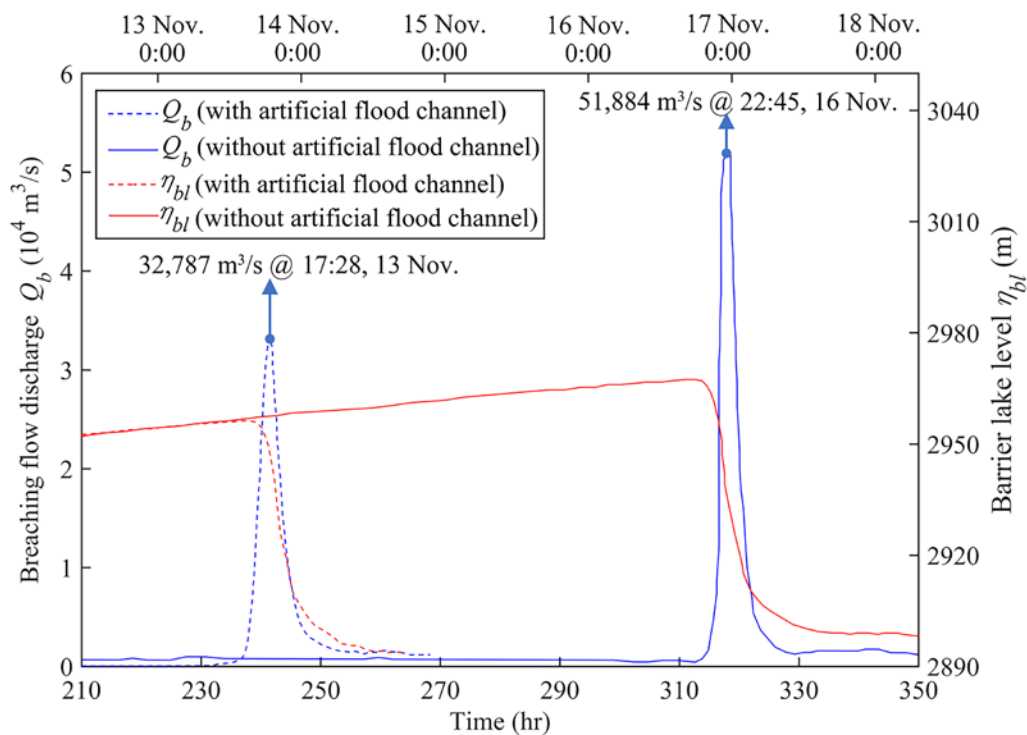
751

752 **Fig. 21.** Model predictions of breaching flow discharge hydrographs (blue) and barrier lake

753 level time series (red): scenario with artificial flood channel (dashed lines); and scenario

754 without an artificial flood channel (solid lines).

755

756   Table 5 summarizes the L^1 values of the model prediction for Baige barrier lake events,

757   which quantitatively demonstrate that the computed results are in good agreement with the

758   measured data. Furthermore, it shows that the error of the numerical solution accumulates

759   and propagates within Phase I, from landslide dam and barrier lake formation, through to

760   barrier lake outburst and downstream flooding, then extending to Phase II, in which a further

761   propagation and accumulation can be observed.

762

763   **Table 5** Summary of L^1 norms of model prediction for Baige barrier lake events

L^1	Phase I	Phase II
Landslide dam morphology L^1_{bd}	12.45%	22.38%
Breaching flow discharge hydrograph $L^1_{Q_b}$	15.31%	23.22%
Flow discharge hydrograph at Yebatan L^1_Q	15.85%	25.47%

764

765   **5. Conclusions**

766   The Baige barrier lake events of 2018 offers unique insight into landslide-induced

767   multi-hazard chains that could produce catastrophic disasters extending far beyond the source

768   zone. Based on a recent 2D double layer-averaged two-phase flow model, we reconstruct the

769   whole process of the Baige barrier lake outburst flood within a single model run,

770   encompassing landslide-generated waves, landslide dam and barrier lake formation, the

771   barrier lake outburst, and the subsequent downstream flood. In terms of landslide-generated

waves, landslide dam morphology, stage time series and discharge hydrographs at the dam site and a downstream gauging station, the present model solutions are in good agreement with field observations. Construction of an artificial flood channel at the dam crest is demonstrated to be an effective mitigation strategy for downstream flood risk arising from a barrier lake outburst. The present work reveals the primary role of grains in landslide dam formation and also the dominant role of water in the barrier lake outburst and the resultant flood. Moreover, whilst small river flow discharge and large initial landslide volume favour landslide dam and barrier lake formation, they delay the occurrence time of the barrier lake outburst and its subsequent flood.

The present modelling framework offers considerable promise for assessing landslide-induced multi-hazard chains, and informing mitigation and adaptation strategies. Such an approach is particularly timely, given the increased instability of high mountain slopes and the accelerating trends in extreme precipitation amount, intensity and frequency of occurrence due to climate change, which are likely to trigger increasing numbers of landslides in the future. The modelling framework would achieve high computational efficiency by implementation of unstructured grids, parallel architecture and adaptive local-time-step techniques, thus supporting timely decision making in emergency response operation. Inevitably, the model incurs uncertainty arising from incomplete knowledge of the estimates of mass exchanges between the landslide and the bed, and interface and bed resistances. Therefore, systematic fundamental investigations are therefore recommended into the mechanisms associated with these exchanges and resistances.

796

797 **References**

798 Abadie, S., Harris, J.C., Grilli, S.T., Fabre, R., 2012. Numerical modeling of tsunami waves

799   generated by the flank collapse of the Cumbre Vieja Volcano (La Palma, Canary Islands):

800   Tsunami source and near field effects. J. Geophys. Res.-Oceans 117, C05030.

801   http://dx.doi.org/10.1029/2011JC007646.

802 ASCE/EWRI Task Committee on Dam/Levee Breaching, 2011. Earthen embankment

803   breaching. J. Hydraul. Eng. 137(12), 1549-1564.

804   https://doi.org/10.1061/(ASCE)HY.1943-7900.0000498.

805 Bandara, S., Soga, K., 2015. Coupling of soil deformation and pore fluid flow using material

806   point method. Comput. Geotech. 63, 199-214.

807   https://doi.org/10.1016/j.compgeo.2014.09.009.

808 Cai, Y., Luan, Y., Yang, Q., Xu, F., Zhang, S., Shi, Y., Yidu, L., 2019. Study on structural

809   morphology and dam-break characteristics of Baige barrier dam on Jinsha River.

810   Yangtze River 50(3), 15-22 (in Chinese).

811 Cao, Z., Pender, G., Wallis, S., Carling, P., 2004. Computational dam-break hydraulics over

812   erodible sediment bed. J. Hydraul. Eng. 130(7), 689-703.

813   http://dx.doi.org/10.1061/(ASCE)0733-9429(2004)130:7(689).

814 Cao, Z., Yue, Z., Pender, G., 2011a. Landslide dam failure and flood hydraulics. Part I:

815   experimental investigation. Nat. Hazards 59(2), 1003-1019.

816   https://doi.org/10.1007/s11069-011-9814-8.

817 Cao, Z., Yue, Z., Pender, G., 2011b. Landslide dam failure and flood hydraulics. Part II:

818   coupled mathematical modelling. Nat. Hazards 59(2), 1021-1045.

819   https://doi.org/10.1007/s11069-011-9815-7.

820 Cao, Z., Yue, Z., Pender, G., 2011c. Flood hydraulics due to cascade landslide dam failure. J.

821   Flood Risk Manag. 4(2), 104-114. https://doi.org/10.1111/j.1753-318X.2011.01098.x.

822 Cao, Z., Xia, C., Pender, G., Liu, Q., 2017. Shallow water hydro-sediment-morphodynamic

823 equations for fluvial processes. J. Hydraul. Eng. 143(5), 02517001.

824 http://dx.doi.org/10.1061/(ASCE)HY.1943-7900.0001281.

825 Carpignano, A., Golia, E., Di Mauro, C., Bouchon, S., Nordvik, J. P., 2009. A methodological

826 approach for the definition of multi-risk maps at regional level: first application. J. Risk

827 Res. 12(3-4), 513-534. https://doi.org/10.1080/13669870903050269.

828 Carrivick, J. L., 2010. Dam break-Outburst flood propagation and transient hydraulics: A

829 geosciences perspective. J. Hydro. 380(3-4), 338-355.

830 https://doi.org/10.1016/j.jhydrol.2009.11.009.

831 Chang, D. S., Zhang, L. M., 2010. Simulation of the erosion process of landslide dams due to

832 overtopping considering variations in soil erodibility along depth. Nat. Hazard Earth Sys.

833 10(4), 933. https://doi.org/10.5194/nhess-10-933-2010.

834 Chen, C., Zhang, L., Xiao, T., He, J., 2020. Barrier lake bursting and flood routing in the

835 Yarlung Tsangpo Grand Canyon in October 2018. J. Hydro. 583, 124603.

836 https://doi.org/10.1016/j.jhydrol.2020.124603.

837 Corominas, J., van Westen, C., Frattini, P., Cascini, L., Malet, J.P., Fotopoulou, S., Catani, F.,

838 Van Den Eeckhaut, M., Mavrouli, O., Agliardi, F. and Pitilakis, K., 2014.

839 Recommendations for the quantitative analysis of landslide risk. Bull. Eng. Geo. Environ.

840 73(2), 209-263. https://doi.org/10.1007/s10064-013-0538-8.

841 Costa, J. E., Schuster, R. L., 1988. The formation and failure of natural dams. Geol. Soc. Am.

842 Bull. 100(7), 1054-1068.

843 https://doi.org/10.1130/0016-7606(1988)100<1054:TFAFON>2.3.CO;2.

844 Cui, P., Zhou, G.G.D., Zhu, X.H., Zhang, J.Q., 2013. Scale amplification of natural debris

845 flows caused by cascading landslide dam failures. Geomorphology 182, 173–189.

846 https://doi.org/10.1016/j.geomorph.2012.11.009.

847 Dai, F. C., Lee, C. F., Deng, J. H., Tham, L. G., 2005. The 1786 earthquake-triggered

848 landslide dam and subsequent dam-break flood on the Dadu River, southwestern China.

849 Geomorphology 65(3-4), 205-221. https://doi.org/10.1016/j.geomorph.2004.08.011.

850 Davies, T. R., Manville, V., Kunz, M., Donadini, L., 2007. Modeling landslide dam break

851 flood magnitudes: case study. J. Hydraul. Eng. 133(7), 713–720.

852 https://doi.org/10.1061/(ASCE)0733-9429(2007)133:7(713).

853 Delaney, K. B., Evans, S. G., 2015. The 2000 Yigong landslide (Tibetan Plateau),

854   rockslide-dammed lake and outburst flood: review, remote sensing analysis, and process

855   modelling. Geomorphology 246, 377-393.

856   https://doi.org/10.1016/j.geomorph.2015.06.020.

857 Donat, M. G., Alexander, L. V., Yang, H., Durre, I., Vose, R., Dunn, R. J. H., ... & Hewitson,

858   B. (2013). Updated analyses of temperature and precipitation extreme indices since the

859   beginning of the twentieth century: The HadEX2 dataset. J. Geophys. Res.-

860   Atmospheres 118(5), 2098-2118. https://doi.org/10.1002/jgrd.50150.

861 Drake, T.G., Shreve, R.L., Dietrich, W.E., Whiting, P.J., Leopold, L.B., 1988. Bedload

862   transport of fine gravel observed by motion-picture photography. J. Fluid Mech. 192,

863   193-217. https://dx.doi.org/10.1017/S0 0221120880 01831.

864 Ermini, L., Casagli, N., 2003. Prediction of the behaviour of landslide dams using a

865   geomorphological dimensionless index. Earth Surf. Proc. Land. 28(1), 31-47.

866   https://doi.org/10.1002/esp.424.

867 Faeh, R., 2007. Numerical modeling of breach erosion of river embankments. J. Hydraul. Eng.

868   133(9), 1000-1009. https://doi.org/10.1061/(ASCE)0733-9429(2007)133:9(1000).

869 Fan, X., Scaringi, G., Korup, O., West, A. J. et al., 2019a. Earthquake-induced chains of

870   geologic hazards: Patterns, mechanisms, and impacts. Rev. Geophys. 57(2), 421-503.

871   https://doi.org/10.1029/2018RG000626.

872 Fan, X., Xu, Q., Alonso-Rodriguez, A. et al., 2019b. Successive landsliding and damming of

873   the Jinsha River in eastern Tibet, China: prime investigation, early warning, and

874   emergency response. Landslides 16(5), 1003-1020.

875   https://doi.org/10.1007/s10346-019-01159-x.

876 Fan, X., Yang, F., Subramanian, S. S. et al., 2020a. Prediction of a multi-hazard chain by an

877   integrated numerical simulation approach: the Baige landslide, Jinsha River, China.

878   Landslides 17(1), 147-164. https://doi.org/10.1007/s10346-019-01313-5.

879 Fan, X., Dufresne, A., Subramanian, S. S., Strom, A. et al. 2020b. The formation and impact

880   of landslide dams–State of the art. Earth-Science Reviews, 103116.

881   https://doi.org/10.1016/j.earscirev.2020.103116.

882 Fread, D. L., 1988. BREACH: an erosion model for earthen dam failure. U.S. Department of

883   Commerce, National Oceanic and Atmospheric Administration, National Weather

884 Service, Office of Hydrology, Silver Spring, USA.

885 Ferguson, R. I., Wathen, S. J., 1998. Tracer-pebble movement along a concave river profile:

886 virtual velocity in relation to grain size and shear stress. Water Resour. Res. 34 (8),

887 2031–2038. http://dx.doi.org/10.1029/98WR01283.

888 Hu, Y., Yu, Z., Zhou, J., 2020. Numerical simulation of landslide-generated waves during the

889 11 October 2018 Baige landslide at the Jinsha River. Landslides, 17, 2317–2328.

890 https://doi.org/10.1007/s10346-020-01382-x.

891 Huang, W., Cao, Z., Yue, Z., Pender, G., Zhou, J. 2012. Coupled modelling of flood due to

892 natural landslide dam breach. Proc. ICE Water Manag. 165, 525-542.

893 https://doi.org/10.1680/wama.12.00017.

894 Lee, C. F., Dai, F. C., 2011. The 1786 Dadu River Landslide Dam, Sichuan, China, in: Evans,

895 S., Hermanns, R., Strom, A., Scarascia-Mugnozza, G. (Eds.), Natural and Artificial

896 Rockslide Dams. Springer, Berlin, Heidelberg, pp. 369-388.

897 https://doi.org/10.1007/978-3-642-04764-0_13

898 Lenzi, M.A., 2004. Displacement and transport of marked pebbles, cobbles and boulders

899 during floods in a steep mountain stream. Hydrol. Process 18 (10), 1899– 1914.

900 http://dx.doi.org/10.1002/hyp.1456.

901 Leonardi, A., Wittel, F. K., Mendoza, M., Vetter, R., Herrmann, H. J., 2016.

902 Particle-fluid-structure interaction for debris flow impact on flexible barriers.

903 Comput-aided Civ. Inf. Eng. 31(5), 323-333. https://doi.org/10.1111/mice.12165.

904 Li, J., Cao, Z., Pender, G., Liu, Q., 2013. A double layer-averaged model for dam-break flows

905 over mobile bed. J. Hydraul. Res. 51(5), 518-534.

906 https://doi.org/10.1080/00221686.2013.812047.

907 Li, J., Cao, Z., Liu, Q., 2019. Waves and sediment transport due to granular landslides

908 impacting reservoirs. Water Resour. Res. 55(1), 495-518.

909 https://doi.org/:10.1029/2018WR023191.

910 Li, J., Cao, Z., Cui, Y., Borthwick, A., 2020. Barrier lake formation due to landslide

911 impacting a river: A numerical study using a double layer-averaged two-phase flow

912 model. Appl. Math. Model. 80, 574-601. https://doi.org/10.1016/j.apm.2019.11.031.

913 Liang, Q., Borthwick, A., 2009. Adaptive quadtree simulation of shallow flows with wet–dry

914 fronts over complex topography. Comput. Fluids 38(2), 221-234.

915   http://dx.doi.org/10.1016/j.compfluid.2008. 02.008.

916   Liu, W., He, S., 2016. A two-layer model for simulating landslide dam over mobile river beds.
917   Landslides 13(3), 565-576. https://doi.org/10.1007/s10346-015-0585-2.

918   Liu, W., He, S., 2018. Dynamic simulation of a mountain disaster chain: landslides, barrier
919   lakes, and outburst floods. Nat. Hazards 90(2), 757-775.
920   https://doi.org/10.1007/s11069-017-3073-2.

921   Miller, G. S., Andy Take, W., Mulligan, R. P., McDougall, S., 2017. Tsunamis generated by
922   long and thin granular landslides in a large flume. J. Geophys. Res.- Oceans 122(1),
923   653-668. http://dx.doi.org/10.1002/2016JC012177.

924   Morris, J. F., 2009. A review of microstructure in concentrated suspensions and its
925   implications for rheology and bulk flow. Rheol. Acta 48(8), 909-923.
926   https://doi.org/10.1007/s00397-009-0352-1.

927   Morris, M. W., Kortenhaus, A., Visser, P. J., 2009. Modelling breach initiation and growth.
928   FLOODsite Report T06-08-02, FLOODsite Project, HR Wallingford, UK.

929   O'Brien, J. S., Julien, P. Y., Fullerton, W. T., 1993. Two-dimensional water flood and mudflow
930   simulation. J. Hydraul. Eng. 119(2), 244-261.
931   https://doi.org/10.1061/(ASCE)0733-9429(1993)119:2(244).

932   Peng, M., Zhang, L. M., 2012. Breaching parameters of landslide dams. Landslides 9(1),
933   13-31. https://doi.org/10.1007/s10346-011-0271-y.

934   Pudasaini, S. P., 2012. A general two-phase debris flow model. J. Geophys. Res.- Earth Surf.
935   117(F3). https://doi.org/0.1029/2011JF002186.

936   Reeks, M. W., Hall, D., 2001. Kinetic models for particle resuspension in turbulent flows:
937   theory and measurement. J. Aerosol Sci. 32(1), 1-31.
938   https://doi.org/10.1016/S0021-8502(00)00063-X.

939   Shan, T., Zhao, J., 2014. A coupled CFD-DEM analysis of granular flow impacting on a
940   water reservoir. Acta Mech. 225(8), 2449-2470.
941   http://dx.doi.org/10.1007/s00707-014-1119-z.

942   Shang, Y., Yang, Z., Li, L., Liao, Q., Wang, Y., 2003. A super-large landslide in Tibet in 2000:
943   background, occurrence, disaster, and origin. Geomorphology 54(3-4), 225-243.
944   https://doi.org/10.1016/S0169-555X(02)00358-6.

945   Shi, C., An, Y., Wu, Q., Liu, Q., Cao, Z., 2016. Numerical simulation of landslide-generated
946   waves using a soil–water coupling smoothed particle hydrodynamics model. Adv. Water
947   Resour. 92, 130-141. https://doi.org/10.1016/j.advwatres.2016.04.002

948   Si, P., Aaron, J., McDougall, S., Lu, J., Yu, X., Roberts, N. J., Clague, J. J., 2018. A
949   non-hydrostatic model for the numerical study of landslide-generated waves. Landslides
950   15(4), 711-726. https://doi.org/10.1007/s10346-017-0891-y.

951   Skvortsov, A., Bornhold, B., 2007. Numerical simulation of the landslide generated tsunami
952   in Kitimat Arm, British Columbia, Canada, 27 April 1975. J. Geophys. Res.- Earth Surf.
953   112, F02028. https://doi.org/10.1029/2006JF000499.

954   Temple, D. M., Hanson, G. J., Neilsen, M. L., Cook, K. R., 2005. Simplified breach analysis
955   model for homogeneous embankments: Part I, Background and model components, in:
956   Proc. 25th Annual U.S. Society on Dams Conference, Denver, pp. 151-161.

957   United States Army Corps of Engineers (USACE), 2016. HEC-RAS, River Analysis System -
958   Hydraulic Reference Manual (Version 5.0).
959   https://www.hec.usace.army.mil/software/hec-ras/documentation.aspx (accessed 23 May
960   2020).

961   Van Asch, T. W., Buma, J., Van Beek, L. P. H., 1999. A view on some hydrological triggering
962   systems in landslides. Geomorphology 30(1-2), 25-32.
963   https://doi.org/10.1016/S0169-555X(99)00042-2.

964   Vetsch, D., Siviglia, A., Ehrbar, D., Facchini, M., Kammerer, S., Koch, A., Peter, S.,
965   Vonwiller, L., Gerber, M., Volz, C., Farshi, D., Mueller, R., Rousselot, P., Veprek, R.,
966   Faeh, R., 2018. System Manuals of BASEMENT, Version 2.8.
967   http://www.basement.ethz.ch (accessed 23 May 2020).

968   Walder, J. S., O'Connor, J. E., 1997. Methods for predicting peak discharge of floods caused
969   by failure of natural and constructed earthen dams. Water Resour. Res. 33(10),
970   2337-2348. https://doi.org/10.1029/97WR01616.

971   Wang, W., Chen, G., Zhang, Y., Zheng, L., Zhang, H., 2017. Dynamic simulation of landslide
972   dam behavior considering kinematic characteristics using a coupled DDA-SPH method.
973   Eng. Anal. Bound. Elem. 80, 172-183.
974   https://doi.org/10.1016/j.enganabound.2017.02.016.

975   Wang, W., Yin, K., Chen, G., Chai, B., Han, Z., Zhou, J., 2019. Practical application of the

coupled DDA-SPH method in dynamic modeling for the formation of landslide dam. Landslides 16(5), 1021-1032. https://doi.org/10.1007/s10346-019-01143-5.

Wang, G., Liu, F., Fu, X., Li, T., 2008. Simulation of dam breach development for emergency treatment of the Tangjiashan Quake Lake in China. Sci. China Technol. Sci. 51(2), 82-94. https://doi.org/10.1007/s11431-008-6019-9.

Wang, Z., Bowles, D. S., 2006a. Three-dimensional non-cohesive earthen dam breach model. Part 1: Theory and methodology. Adv. Water Resour. 29(10), 1528-1545. https://doi.org/10.1016/j.advwatres.2005.11.009.

Wang, Z., Bowles, D. S., 2006b. Three-dimensional non-cohesive earthen dam breach model. Part 2: Validation and applications. Adv. Water Resour. 29(10), 1490-1503. https://doi.org/10.1016/j.advwatres.2005.11.010.

Wilcock, P. R., 1997. Entrainment, displacement and transport of tracer gravels. Earth Surf. Proc. Land. 22 (12), 1125–1138. http://dx.doi.org/10.1002/(SICI) 1096-9837(199712)22:12 <1125 .

Worni, R., Huggel, C., Clague, J. J., Schaub, Y., Stoffel, M., 2014. Coupling glacial lake impact, dam breach, and flood processes: A modeling perspective. Geomorphology 224, 161-176. https://doi.org/10.1016/j.geomorph.2014.06.031.

Wu, W., 2013. Simplified physically based model of earthen embankment breaching. J. Hydraul. Eng. 139(8), 837-851. https://doi.org/10.1061/(ASCE)HY.1943-7900.0000741.

Wu, W., Marsooli, R., He, Z., 2012. Depth-averaged two-dimensional model of unsteady flow and sediment transport due to noncohesive embankment break/breaching. J. Hydraul. Eng. 138(6), 503-516. https://doi.org/10.1029/2017WR022492.

Wu, Y., Fang, H., Huang, L., Ouyang, W., 2020. Changing runoff due to temperature and precipitation variations in the dammed Jinsha River. J. Hydrol. 582, 124500. https://doi.org/10.1016/j.jhydrol.2019.124500.

Xu, Q., Fan, X. M., Huang, R. Q., Van Westen, C., 2009. Landslide dams triggered by the Wenchuan Earthquake, Sichuan Province, south west China. Bull. Eng. Geol. Environ. 68(3), 373-386. https://doi.org/10.1007/s10064-009-0214-1.

Xu, W. J., Yao, Z. G., Luo, Y. T., Dong, X. Y., 2020. Study on landslide-induced wave disasters using a 3D coupled SPH-DEM method. Bull. Eng. Geol. Environ. 79(1), 467-483. https://doi.org/10.1007/s10064-019-01558-3.

1007   Xu, Y., Zhang, L. M., 2009. Breaching parameters for earth and rockfill dams. J. Geotech.

1008   Geoenviron. Eng. 135(12), 1957-1970.

1009   https://doi.org/10.1061/(ASCE)GT.1943-5606.0000162.

1010   Zhao, T., Dai, F., Xu, N. W., 2017. Coupled DEM-CFD investigation on the formation of

1011   landslide dams in narrow rivers. Landslides 14(1), 189-201.

1012   https://doi.org/10.1007/s10346-015-0675-1.

1013   Zhang, L., Xiao, T., He, J., Chen, C., 2019. Erosion-based analysis of breaching of Baige

1014   landslide dams on the Jinsha River, China, in 2018. Landslides 16(10), 1965-1979.

1015   https://doi.org/10.1007/s10346-019-01247-y.

1016   Zhang, Y., Meng, X. M., Dijkstra, T. A., Jordan, C. J., Chen, G., Zeng, R. Q., Novellino, A.,

1017   2020. Forecasting the magnitude of potential landslides based on InSAR techniques.

1018   Remote Sens. Environ. 241, 111738. https://doi.org/10.1016/j.rse.2020.111738.

1019   Zhang, Z., He, S., Liu, W., Liang, H., Yan, S., Deng, Y., Bai, X. Chen, Z., 2019. Source

1020   characteristics and dynamics of the October 2018 Baige landslide revealed by broadband

1021   seismograms. Landslides 16(4), 777-785. https://doi.org/10.1007/s10346-019-01145-3

1022   Zhong, Q., Chen, S., Wang, L., Shan, Y., 2020. Back analysis of breaching process of Baige

1023   landslide dam. Landslides, in press. https://doi.org/10.1007/s10346-020-01398-3

1024   Zitti, G., Ancey, C., Postacchini, M., Brocchini, M., 2016. Impulse waves generated by snow

1025   avalanches: momentum and energy transfer to a water body. J. Geophys. Res.- Earth Surf.

1026   121(12), 2399-2423. https://doi.org/10.1002/2016JF003891.

1027

List of figure captions

Fig. 1. Location of Baige barrier lake, Jinsha River, China (adapted from Fan et al., 2020a): (a) upstream areas inundated by barrier lake; (b) towns affected by downstream flooding (the orange box indicates the study area).

Fig.2. "10.10" Baige barrier lake: (a) formation; (b) after breaching. (photo courtesy of Chinanews.com).

Fig. 3. "11.03" Baige barrier lake: (a) formation; (b) with artificial flood channel; (c) during breaching; (d) after breaching (photo courtesy of a CCTV.com; b Red Star News; c Ministry of Emergency Management of China; d L. Zhang et al., 2019).

Fig. 4. Phase I "10.10" Baige landslide impacting Jinsha river: model predictions of landslide velocity field at times $t =$ (a) 5 s, (b) 10 s, (c) 20 s, (d) 40 s, (e) 100 s, and (f) 900 s.

Fig. 5. Phase I "10.10" Baige landslide-generated waves: predicted water level hydrographs at three locations in the Jinsha river near Baige, Sichuan, China.

Fig. 6. "10.10" Baige landslide dam geometry: (a) bed deformation at $t =$ 900 s predicted by present model; and (b) cross-section profile of landslide dam in the original river stream-wise direction (A-A'): model prediction (solid line) and measured data from Fan et al. (2020a) (dashed line).

Fig. 7. "10.10" Baige landslide dam and barrier lake formation: (a1-a6) depth of water layer; (b1-b6) landslide thickness; and (c1-c6) bed deformation.

Fig. 8. (a) Breaching flow discharge hydrograph and (b) flow discharge hydrograph and sediment volume output time series at the Yabatan gauging station: model predictions (solid lines) and measured data from Cai et al. (2019) (open black circles).

Fig. 9. Water level time series at the barrier lake and selected sites downstream of the "10.10"

Baige landslide dam.

Fig. 10. "10.10" Landslide-induced barrier lake outburst and the resultant flood: (a1-a6)

depth of water layer; (b1-b6) water-sediment mixture thickness; and (c1-c6) bed deformation.

(a1, b1 and c1) Landslide dam is overtopped naturally and dam breach commences. (a2, b2

and c2) Breaching flow arrives at Yebatan. (a3, b3 and c3) Breaching flow discharge is

almost equivalent to upstream inflow discharge. (a4, b4 and c4) Breaching flow peaks. (a5,

b5 and c5) Peak breaching flow arrives at Yebatan. (a6, b6 and c6) Jinsha river resumes its

base flow and the dam breach process terminates.

Fig. 11. Contour plots of velocity difference between water and sediment phases of the

water-sediment mixture flow layer in the transverse (y – axis) direction at different times

from 10 s to 55.75 hr after the start of the "10.10" Baige landslide: a1–a5 with $d = 1$ mm;

and b1–b5 with $d = 20$ mm.

Fig. 12. Contour plots of velocity difference between water and sediment phases of the

water-sediment mixture flow layer in the longitudinal (x – axis) direction at different times

from 10 s to 55.75 hr after the start of the "10.10" Baige landslide, a1-a5 with $d = 1$ mm,

and b1-b5 with $d = 20$ mm.

Fig. 13. Model predictions of breaching flow discharge hydrographs for three different Jinsha

river inflow discharges.

Fig. 14. Model predictions of breaching flow discharge hydrographs for three different initial

landslide volumes.

Fig. 15. "10.10" Baige landslide dam morphology assuming different bed friction coefficient

$\tan\delta$ (a1-a3) bed deformation at $t = 900$ s predicted by present model; and (b1-b3)

cross-section profile of landslide dam in the original river stream-wise direction (A-A'):

model prediction (solid line) and measured data from Fan et al. (2020a) (dashed line).

1090

Fig. 16. "10.10" Baige landslide dam morphology assuming different Manning roughness

coefficient n_b (a1-a3) bed deformation at $t =$ 900 s predicted by present model; and (b1-b3)

cross-section profile of landslide dam in the original river stream-wise direction (A-A'):

model prediction (solid line) and measured data from Fan et al. (2020a) (dashed line).

1095

Fig. 17. Model predictions (solid lines) of breaching flow discharge hydrographs assuming (a)

different bed friction coefficient $\tan\delta$; and (b) different Manning roughness coefficient n_b

and measured data (open circles) from Cai et al. (2019).

1099

Fig. 18. "11.03" Baige landslide dam geometry: (a) predicted bed deformation contours at

$t =$ 900 s; and (b) predicted (solid line) and measured (dashed line, Fan et al. 2020a)

cross-sectional profiles of the landslide dam in a longitudinal direction along the river (B-B').

1103

Fig. 19. (a) Breaching flow discharge hydrograph and water level time series at the "11.03"

Baige landslide dam site; (b) flow discharge hydrograph and sediment volume output series

at Yebatan (the downstream station): model predictions (solid lines) and measured data (open

circles).

1108

Fig. 20. "11.03" Baige landslide dam breach evolution depicted as bed deformation contours

and superimposed flow velocity vectors at post-landslide times, $t =$: (a) 202.75 hr; (b)

206.75 hr; (c) 230.75 hr; (d) 235.75 hr; (e) 240.2 hr; and (f) 260.0 hr.

1112

Fig. 21. Model predictions of breaching flow discharge hydrographs (blue) and barrier lake

level time series (red): scenario with artificial flood channel (dashed lines); and scenario

without an artificial flood channel (solid lines).

1116

1117

List of table captions

Table 1 "10.10" Baige landslide-generated wave run-up on the opposite bank

Table 2 Summary of "10.10" Baige landslide dam morphology

Table 3 Predicted effect of inflow discharge on landslide dam formation, overtopping, and breaching processes (Series 1 tests)

Table 4 Predicted effect of inflow landslide volume on landslide dam formation, overtopping, and breaching processes (Series 2 tests)

Table 5 Summary of L^1 norms of model prediction for Baige barrier lake events